Physics of Fluids

Turbulence structure in a very sharp thermally stratified open-channel meander

Cite as: Phys. Fluids **34**, 035130 (2022); https://doi.org/10.1063/5.0083230
Submitted: 23 December 2021 • Accepted: 02 March 2022 • Published Online: 21 March 2022

Duy Nguyen, Michael P. Kirkpatrick, N. Williamson, et al.

Physics of Fluids ARTICLE scitation.org/journal/phf

Turbulence structure in a very sharp thermally stratified open-channel meander

Cite as: Phys. Fluids **34**, 035130 (2022); doi: 10.1063/5.0083230
Submitted: 23 December 2021 · Accepted: 2 March 2022 ·
Published Online: 21 March 2022

View Online Export Citation CrossMark

Duy Nguyen,[1,a)] Michael P. Kirkpatrick,[1] N. Williamson,[1] S. W. Armfield,[1] and W. Lin[2]

AFFILIATIONS

[1]School of Aerospace, Mechanical and Mechatronic Engineering, The University of Sydney, Sydney, Australia
[2]College of Science and Engineering, James Cook University, Townsville, Australia

[a)]Author to whom correspondence should be addressed: duy.nguyen1@sydney.edu.au

ABSTRACT

Direct numerical simulation (DNS) results for turbulent open-channel flow through an idealized sine-generated meander with and without an internal heat source that models radiative heating from above are used to analyze the effect of a very sharp meander configuration and thermal stratification on the turbulence structure in the channel with friction Reynolds number $Re_\tau = 200$. Spatial distributions of temperature, mean velocities, vorticity, mean-flow kinetic energy, and turbulent kinetic energy (TKE) are presented. In both cases, the cross-sectional motion is characterized by three circulation cells: a center-region cell and two weaker outer bank and inner bank cells. However, there is also a small cell observed near the corner of the channel bed inner bank at the channel outlet and the channel bed outer bank at the channel inlet. The tri-cellular cross-stream motions control the distributions of temperature and kinetic energy. In the stratified case, two separated shear layers (SSLs) are found: the first one is formed before the bend apex, and the second one is observed in the wake after the bend apex. In the neutral case, only the first SSL is observed. Turbulent amplification can be seen in both cases; however, in the stratified case, the second SSL stretches out to the channel outlet and is introduced back to the channel inlet by an anti-symmetric periodic boundary condition and then follows the outer bank line. The two SSLs converge in the region before the bend apex and amplify the turbulence more strongly there than in the neutral case. The turbulence kinetic energy budget terms for the stratified case are analyzed to determine the characteristics of production, dissipation and transport of TKE in thermally stratified meandering flow.

I. INTRODUCTION

In this study, we present direct numerical simulation (DNS) results for meandering open channel flow with and without radiative heating through the upper surface. Radiative heating is modeled as a volumetric heat source that decays exponentially with depth, while the meander geometry is modeled using a sine-generated curve.

Our study is the first to report the turbulence characteristics in radiatively driven thermally stratified open-channel meanders. Little is known about the turbulence structure in stratified open-channel meanders. The main goal of this paper is to present detailed numerical data on the turbulent flow in an open-channel meander with and without radiatively driven thermal stratification, including mean flow velocity and temperature fields, and the dominant turbulent kinetic energy (TKE) budget terms.

In isothermal curved open-channel flow, one of the key features is the existence of secondary flow cells perpendicular to the main flow direction. The imbalance between the depth-varying radial acceleration (due to the depth-varying streamwise velocity) and the barotropic pressure gradient leads to a strong central lateral secondary circulation. Other smaller secondary circulations, including an outer bank cell and inner bank cell, can also occur (Boussinesq, 1868; Thompson, 1876). The two cells can be found in Fig. 1.

The outer bank cell has been the subject of several recent studies in non-stratified flow through bends including those of Blanckaert and de Vriend (2004, 2005a), van Balen *et al.* (2009), and Farhadi *et al.* (2018). Although relatively small and weak, this outer bank cell is known to play an essential role concerning the stability of the outer bank (Bathurst, 1977; Blanckaert and Graf, 2001).

Turbulence plays a vital role in the formation of these cross-stream circulation cells. Lateral circulations have been shown to significantly affect the distribution of both mean velocities and turbulent shear stresses within the river (Blanckaert, 2010). Kim *et al.* (2020) report a recirculation zones in both inner and outer bank of a meander in which affect the intensity of streamwise and spanwise velocities. The mechanisms underlying the lateral circulation cells are revealed by the streamwise vorticity equation, which shows that the centrifugal

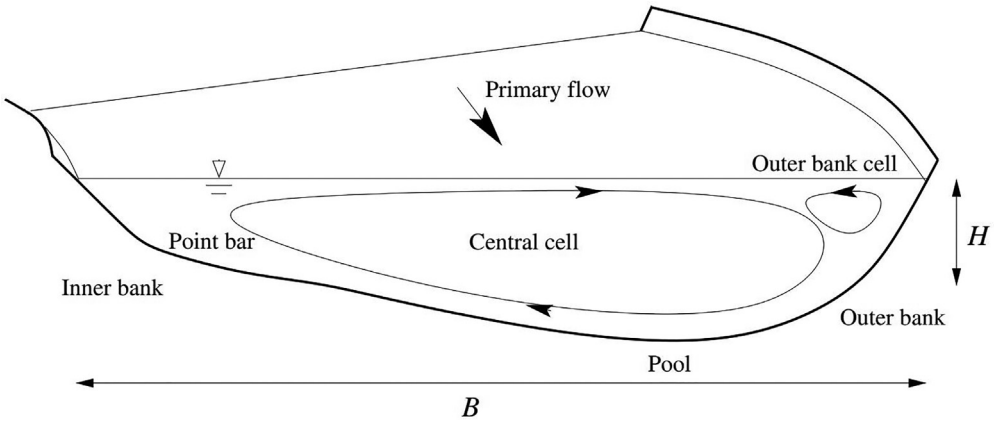

FIG. 1. Flow in a typical river bend showing secondary central and outer bank circulations.

force and the cross-stream turbulent stresses play a dominant role (Blanckaert and de Vriend, 2004).

The outer bank cell is enhanced by kinetic energy input from turbulence and, at the same time, suppressed by turbulent dissipation. Although the kinetic energy transfer from turbulence to the mean flow is small compared to the total energy losses, it is essential for the generation of the outer bank cell (Blanckaert and de Vriend, 2004). van Balen *et al.* (2009) showed this cell to be a result of the spatial distribution of turbulence stresses and centrifugal forcing.

Turbulence characteristics in a sharp open-channel bend for non-stratified flow have been studied thoroughly by Blanckaert and de Vriend (2005a), where the distributions of TKE, its production, and some parameters characterizing the turbulence structure are measured and evaluated. Results show that there is a reduction of turbulence activity in the outer bend, and the main cause for that is that the Reynolds stress tensor is more diagonally dominant. Similar findings by Esfahani and Keshavarzi (2020) show the cross-stream turbulence anisotropy considerably strengthen TKE near all bank cells. However, a numerical study by Constantinescu *et al.* (2011) found that several strong streamwise-oriented vortices (SOVs) and large separated shear layers (SSLs) form near the high-curvature inner bank. Those vortices are the reason for turbulence amplification in this region.

There are very few studies in the literature investigating stratified flows in open-channel meanders. Equilibrium states of turbulent stably stratified straight open-channel flow under different conditions subjected to short-wave heating have been presented by Williamson *et al.* (2015). For curved flow, there are existing field studies in estuaries by Chant and Wilson (1997), Lacy and Monismith (2001), Nidzieko *et al.* (2009), and Pein *et al.* (2018), and a numerical study of two-layered density stratified flow through a bend with rectangular cross-section by Williamson *et al.* (2012). Those studies described the typical flow occurring in estuaries, which involves a layer of freshwater flowing above a lower layer of salt water, with a relatively sharp interface between the two layers. Density stratification also occurs in rivers, canals, and shallow seas under the influence of solar heating. The results of those studies have shown that stratification can strengthen the secondary circulation by strengthening the vertical shear in the stream-wise flow and reducing the frictional damping by reducing turbulence. Hence, stratification can produce a similarly more pronounced variation in centrifugal forcing and circulation strength. Kranenburg *et al.* (2019) show the difference in the central circulation size between stronger stratification of ebb tides and the weaker stratification of flood tides in a sharp estuarine bend. However, another study by Chant and Wilson (1997) showed that sufficiently strong stratification will suppress the circulation, as the secondary circulation generates a buildup of denser fluid in the inner bend, thus inducing a baroclinic pressure gradient force (BCPG) counteracting the classical secondary circulation.

In rivers, the presence of thermal stratification due to solar heating inhibits mixing, resulting in reduced oxygen in the lower layers of the river as well as the accumulation of contaminants and nutrients—conditions that have been found to cause long-term damage to the ecosystems (Vant, 1987; Turner and Erskine, 2005). Reduced flow rates can also lead to acute damage events such as cyanobacterial outbreaks (algal blooms) and mass fish kills. These events are associated with thermal stratification, solar radiation intensity, low river flow rate, and hot/still weather conditions (Sherman *et al.*, 1998; Bormans *et al.*, 2004). A sudden breakdown of thermal stratification was found to be the main cause of two recent fish kills in the Darling River system in southeastern Australia (Moritz *et al.*, 2019).

A motivation for this study is to make progress toward a greater understanding of the effects of meander bends on thermal stratification in rivers. The results presented in this study are for an idealized geometry and are at a low Reynolds number due to the high computational requirements imposed by the use of direct numerical simulation on a large spatial domain. Nevertheless, they represent a first step toward this goal. Another goal of this paper is to analyze the turbulence activity near the bend apex that results in turbulence amplification and compare neutral and thermally stratified open-channel flows through a sharp meander.

An outline of the present paper is as follows. Section II describes the meander model used. Section III presents the problem formulation, including the governing equations and non-dimensionalizations used. The direct numerical simulation (DNS) code and details of the numerical simulations, including the curvilinear grid transformation, are

given in Sec. IV. After a brief observation and comparison in Sec. V, in Sec. VI, we present flow visualizations of mean flow velocity and vorticity. The temperature field is discussed in Sec. VII. Section VIII describes the distribution of TKE and gives a term-by-term analysis of the TKE transport equation. Finally, Sec. IX summarizes the central findings of the paper and makes some concluding remarks.

II. GEOMETRY MODEL

The sine-generated curve (SGC) presented by Leopold and Langbein (1966) is used here as an idealized description of river meander topology. The planform meander geometry is shown in Fig. 2. The model defines the variation in the deviation angle $\theta(s)$ relative to the meander belt axis at a location s along the meander centerline as

$$\theta(s) = \theta_0 \cos 2\pi \frac{s}{L}. \tag{1}$$

This can be formulated in terms of local radius of curvature $R(s)$ as

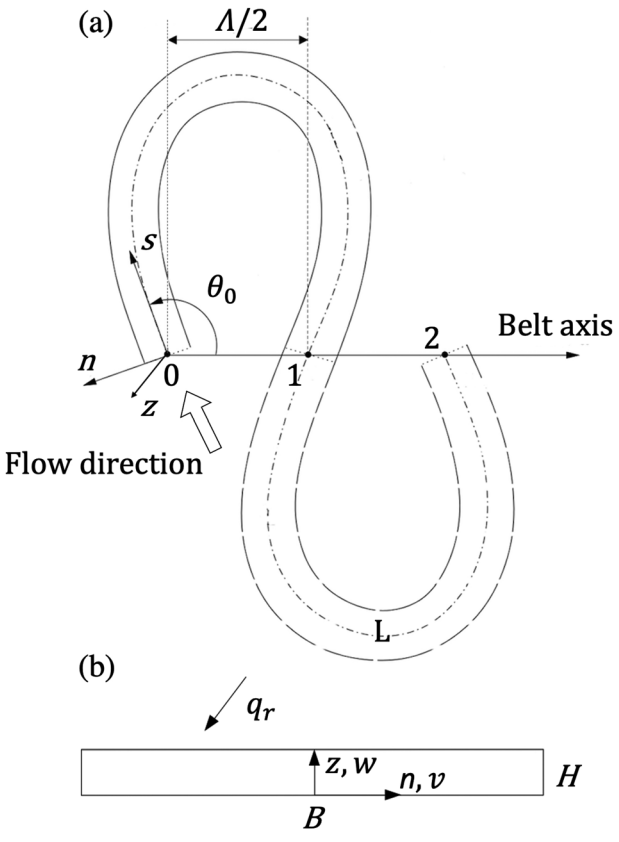

FIG. 2. Schematic of simulation domain. (a) Planform view of meander geometry and (b) its transverse cross-section. The curvilinear coordinate directions are n, s, and z, while θ_0 is the maximum deviation angle, Λ the meander wavelength, L the meander path length, defined as the total distance along the meander centerline between points 0 and 2, B the meander width, H the channel depth, and q_r the radiative heat source. The simulation is conducted on a half meander wavelength from point 0 to point 1.

$$\frac{1}{R(s)} = -2\pi \frac{\theta_0}{L} \sin 2\pi \frac{s}{L}. \tag{2}$$

Here, θ_0 is the maximum deviation angle with respect to the axis of the meander belt and L the meander path length defined as the total distance along the meander centerline (from point 0 to 2 on Fig. 2). Leopold and Langbein (1970) compared this model to a number of real meanders and found that it gives a good idealized representation of naturally occurring meanders.

We set a very sharp bend of $H/R_{min} = 0.075$, and the shallowness B/H is set equal to 10, which gives us an aspect ratio $R_{min}/B = 1.33$ for our study, where R_{min} is the minimum radius of curvature, which occurs at the meander apex. High values of $\theta_0 = 110°$ characterize a meander close to the cutoff after which an ox-bow lake typically forms. Using Eq. (2), the ratio of L/B then equals 16.08, which is supported by Ferguson (1975), who found a consistent average ratio of L/B approximately of 20 for a sample of 19 rivers. The remaining ratio of meander wavelength to width is $\Lambda/B = 4.35$. The relative importance of the mechanisms for lateral redistribution of streamwise momentum along the bend depends on the parameters $C_f^{-1}H/R$ and B/R, where C_f is the Chézy friction coefficient. These parameters are both small in mildly curved bends but $O(1)$ in sharp bends (Blanckaert and de Vriend, 2010).

III. PROBLEM FORMULATION

Using the sine-generated curve, the channel has a rectangular cross-section with no-slip walls at the lower surface and sidewalls, an adiabatic, free-slip impermeable boundary at the upper surface, and "anti-symmetric" periodic boundaries in the streamwise directions. Anti-symmetric periodic boundaries are similar to a periodic boundary condition, except that they mirror in the cross-stream direction (Segal *et al.*, 1994). As such, our domain represents half of a full S-shaped meander, with the half meander length from point 0 to point 1 in Fig. 2. The flow is driven by a constant pressure gradient in the streamwise direction.

The problem is cast in non-dimensional form by non-dimensionalizing in terms of a length scale $\tilde{\delta}$ that is equal to the channel height, a velocity scale $\tilde{u}_\tau$ equal to the average friction velocity on the bottom surface and sidewalls, and a temperature scale $\tilde{\Phi}_N$ associated with the radiative forcing. Throughout this paper, dimensional quantities are indicated by a tilde, while non-dimensional quantities have no tilde.

Following Williamson *et al.* (2015), radiative heating is modeled by a depth-dependent volumetric heat source $\tilde{q}_r(\tilde{z})$ following the Beer–Lambert law:

$$\tilde{q}_r(\tilde{z}) = \tilde{I}_s \tilde{\alpha} e^{(\tilde{z}-\tilde{\delta})\tilde{\alpha}}, \tag{3}$$

where $\tilde{I}_s$ is the short-wave radiative heat flux through the upper surface and $\tilde{\alpha}$ an attenuation coefficient.

A non-dimensional heat source, q_e, can be derived as

$$q_e = \frac{\tilde{q}_r - \tilde{Q}_r}{\tilde{Q}_N}, \tag{4}$$

where

$$\tilde{Q}_r = \frac{1}{\tilde{\delta}} \int_0^{\tilde{\delta}} \tilde{q}_r(\tilde{z}) d\tilde{z} \tag{5}$$

and

$$\tilde{Q}_N = \frac{1}{\tilde{\delta}^2}\int_0^{\tilde{\delta}} (\tilde{Q}_r - \tilde{q}_r(\tilde{z}))(\tilde{\delta} - \tilde{z})d\tilde{z}. \tag{6}$$

Subtracting the domain-averaged heat source $\tilde{Q}_r$ ensures that the global heat source is zero, and hence, that the domain-averaged temperature remains constant over time.

This gives a temperature scale based on the radiative heat flux

$$\tilde{\Phi}_N = \frac{\tilde{Q}_N\tilde{\delta}}{\tilde{\rho}_b\tilde{c}_p\tilde{u}_\tau}, \tag{7}$$

where $\tilde{\rho}_b$ and $\tilde{c}_p$ are a reference density and the specific heat of the fluid.

The flow is governed by the Oberbeck–Boussinesq form of equations for conservation of mass, momentum, and energy for an incompressible fluid. In non-dimensional coordinate free form, these equations are as follows:

$$\nabla.\mathbf{u} = 0, \tag{8}$$

$$\frac{\partial \mathbf{u}}{\partial t} + \nabla.(\mathbf{uu}) = -\nabla p + \frac{1}{Re_\tau}\nabla^2\mathbf{u} - \frac{\partial p}{\partial s}\mathbf{e}_s + \lambda\phi\mathbf{e}_z, \tag{9}$$

$$\frac{\partial \phi}{\partial t} + \nabla.(\mathbf{u}\phi) = \frac{1}{Re_\tau Pr}\nabla^2\phi + q_e. \tag{10}$$

Here, $\mathbf{u}$, t, and p are the dimensionless velocity, time, and pressure, respectively, and ϕ is the dimensionless temperature. $\mathbf{e}_s$ and $\mathbf{e}_z$ are unit vectors in the streamwise (s) and vertical (z) directions. The Prandtl number $Pr = \tilde{\nu}/\tilde{\sigma}$ where $\tilde{\sigma}$ is the thermal diffusivity of the fluid and $\tilde{\nu}$ is the fluid viscosity. The Reynolds number $Re_\tau = \tilde{u}_\tau\tilde{\delta}/\tilde{\nu}$ and the dimensionless buoyancy coefficient λ,

$$\lambda = \frac{\tilde{\beta}\tilde{g}\tilde{\Phi}_N\tilde{\delta}}{\tilde{u}_\tau^2}, \tag{11}$$

where $\tilde{\beta}$ is the coefficient of thermal expansion and $\tilde{g}$ gravity. We refer the reader to Kirkpatrick *et al.* (2020) for further details of the non-dimensionalization scheme.

The stream-wise boundaries at $s = 0$ and $s = L$ are anti-symmetric periodic boundaries as described above. The boundary conditions for the bottom ($z = 0$) no-slip adiabatic wall, stress-free adiabatic top boundary ($z = 1$), and lateral boundaries of no-slip adiabatic sidewalls ($n = -5$ and $n = 5$) are

$$z = 0: \quad u = v = w = 0; \quad \frac{\partial \phi}{\partial z} = 0, \tag{12}$$

$$z = 1: \quad \frac{\partial u}{\partial z} = \frac{\partial v}{\partial z} = 0; \quad w = 0; \quad \frac{\partial \phi}{\partial z} = 0, \tag{13}$$

$$n = -5, n = 5: \quad u = v = w = 0; \quad \frac{\partial \phi}{\partial n} = 0. \tag{14}$$

Williamson *et al.* (2015) show that for a doubly periodic straight channel, the effects of stable stratification on the flow are a function of the non-dimensional buoyancy coefficient λ. Another parameter that determines the behavior and turbulence properties of the flow is the friction Richardson number Ri_τ, which can be written in terms of our non-dimensional variables as

$$Ri_\tau = \frac{\lambda\Delta\phi H}{u_\tau^2}. \tag{15}$$

Here, $\Delta\phi = \phi_t - \phi_b$, where ϕ_t and ϕ_b are the horizontally and time-averaged temperature at the channel top and bottom, and $u_\tau = \tilde{u}_\tau/\tilde{u}_\tau = 1$.

Ri_τ is a bulk parameter that represents the ratio between stabilizing effects of temperature stratification and destabilizing effects of shear at walls and is a useful bulk parameter for characterizing buoyancy effects of stratified channel flow (Garg *et al.*, 2000; García-Villalba and del Álamo, 2011). For destratifying flow that occurs when the radiative heat source is removed, Kirkpatrick *et al.* (2019) show that the destratification rate is a function of Ri_τ. The strength of the mean flow relative to stratification can be assessed via the bulk internal Froude number, defined by

$$Fr' = \frac{U_{bulk}}{N_{max}H}, \tag{16}$$

where U_{bulk} is the bulk streamwise velocity and N_{max} is the maximum value of N in the channel. Here, $N = (\lambda\partial\bar{\phi}/\partial z)^{1/2}$ is the buoyancy frequency, where $\bar{\phi}$ is the time average temperature field, see Nidzieko *et al.* (2009) for a similar approach.

IV. METHOD

Simulations were performed using the PUFFIN code to solve Eqs. (8)–(10). The PUFFIN code has been developed by Kirkpatrick (2002) for large eddy simulation (LES) and has been validated for DNS of turbulent stratified flows against other published correlations and scaling relationships (Kirkpatrick *et al.*, 2019, 2020). The flow case parameters for both simulations analyzed in this paper can be found in Table I. The Reynolds number used is the highest that could be achieved on this very large domain with computing resources available to us. The Prandtl Pr number is set to unity and represents a canonical case where thermal diffusivity equals momentum diffusivity. A higher Prandtl number would require a higher resolution and computational cost. The absorption coefficient is typical of moderately turbid rivers. To get a neutral case, we set the dimensionless buoyancy coefficient $\lambda = 0$. As such, the neutral case has no density stratification and, therefore, no buoyancy effects. For the density stratified case, a value of $\lambda = 0.5$ was chosen based on preliminary investigations, which indicated that this degree of stratification leads to a significant modification of the flow morphology while maintain fully turbulent flow. At $\lambda = 1$ and $Re_\tau = 200$, the flow becomes laminar over large regions of the domain.

In the cross-stream direction, the grid cell sizes in viscous wall units are $\Delta n^+ = 3.9$ from $n = -4.5$ to $n = 4.5$, contracting to $\Delta n^+ = 0.5$ at the walls. In the vertical direction, $\Delta z^+ = 3.9$ for $z = 0.2$–0.8 and is refined close to the upper and lower surfaces so that $\Delta z^+ = 0.5$ at the bottom boundary and $\Delta z^+ = 1$ at the upper

TABLE I. Simulation parameters cases without ($\lambda = 0.0$) and with ($\lambda = 0.5$) radiatively driven thermal stratification.

Cases	λ	Re_τ	Pr	$\tilde{\alpha}\tilde{\delta}$	Ri_τ	Fr'
1	0.0	200	1	8	0.0	∞
2	0.5	200	1	8	10.21	0.39

boundary. In the s direction, $\Delta s^+ = 3.9$ in the middle of the channel throughout the meander length. However, the variation in the streamwise grid cell dimension is a function of curvature. At the bend apex, from the middle of the channel, grid cell dimension expands to $\Delta s^+ = 5.5$ at the outer bank and contracts to $\Delta s^+ = 2.4$ close to the inner bank. At the channel inlet and outlet where the curvature is zero, Δs^+ stays as 3.9 for the whole channel width.

This resolution is similar to the resolution used in other DNS studies in the published literature that use fourth-order finite-volume/finite-difference schemes. See for example the study by Komen *et al.* (2017), who note that typical DNS mesh resolution using finite difference schemes for straight channel flow is $\Delta^+ = 9$ in the streamwise direction, $\Delta^+ = 4.5$ in the spanwise direction, and Δ^+ from 0.5 at the wall to 4.5 in the outer region in the wall normal direction.

The computational domain was meshed using an orthogonal, curvilinear coordinate system with velocity vectors represented using physical components and a staggered grid arrangement. The mesh has approximately 178 million cells ($4032 \times 582 \times 76$ points in the streamwise, spanwise, and vertical directions, respectively). The curvilinear grid is obtained by using a transformation that maps computational $\xi - \eta - \zeta$ coordinates to physical $s - n - z$ coordinates. The transformation is achieved using a series of 20 quintic Hermite spline segments with control points located along the sine-generated curve defining the centerline of the channel. The n and z lines are straight and orthogonal to the curved s coordinate lines. The transformation is a fully transformed finite volume scheme, with component-wise averaged contravariant physical components used as the dependent variables.

To check for grid independence, an independent simulation was run using a grid with spatial and temporal resolution equal to half that used for the simulation presented in this paper. A comparison of some key first- and second-order bulk parameters is shown in Table II, including the bulk velocity, U_{bulk}, the domain-averaged mean flow kinetic energy, KE_D; the domain-averaged turbulent kinetic energy, TKE_D; and the friction Richardson number, Ri_τ. The maximum difference between the two simulations is less than 2%, indicating that good spatial convergence has been achieved. In the remainder of this paper, results are presented for simulations using the fine grid resolution, which, as discussed above, is similar to that typically used for DNS of similar flows.

The spatial discretization uses fourth-order central differences for the advection terms in the momentum and energy equations. All other terms in the momentum, energy, and pressure correction equations are discretized using second-order central differences. The equations are integrated in time using a second-order accurate fractional step method. Simulations were performed at conditions for an initial spin-up period of 100 non-dimensional time units on a coarse mesh using cells with approximately twice the size of the fine mesh in all directions. A non-dimensional time unit is defined as $t = (\tilde{t} \times \tilde{u_\tau})/\tilde{\delta}$.

TABLE II. Grid sensitivity for bulk parameters. Here, KE_D and TKE_D are domain-averaged values of the mean flow kinetic energy and turbulent kinetic energy, respectively.

Resolution	U_{bulk}	KE_D	TKE_D	Ri_τ
Coarse grid	13.49	101.12	2.39	10.19
Fine grid	13.49	99.33	2.39	10.21

After that, the solution was interpolated onto the fine grid and set to run for a transitional period of 10 non-dimensional time units. In these two periods, the pressure gradient was varied dynamically until it gives the required average friction velocity. The average friction velocity is defined as the average over the bottom surface and side walls of the channel. At this point, inspection of time series of bulk parameters such as average friction velocity, bulk velocity, and streamwise pressure gradient indicated that the flow had reached a statistically steady state. The time step was then fixed at a constant value of $\Delta t = 1 \times 10^{-4}$, which ensures that the maximum Courant number ($\Delta t u_i/\Delta x_i$) in the domain remains approximately 0.2. Here, Δx_i is the cell width in the direction of the velocity component u_i. The pressure gradient was fixed at $\partial p/\partial s = -1.51$, which is the value determined by the dynamic variation procedure described above. The bulk velocity has an average value of $U_{bulk} = 13.49$, which gives the rate at which mechanical work is supplied per unit volume as $w_p = -U_{bulk}\partial p/\partial s = 20.24$. The simulation was then run for an extra 2 time units before starting a 30 time unit run in which flow data were collected.

Data collection involved recording a time series for each dependent variable on a 3D array of "probes." This was done to avoid exorbitant storage requirements that would be involved if time series data were recorded at every grid node. Probes were distributed on a 31×81 grid in the n and s directions, respectively, as shown in Fig. 3. In the z direction, probes were located at every layer of the computational mesh. To enable the calculation of spatial gradients, each probe measures data on a horizontal stencil of neighboring nodes. Data were recorded every 10 time steps. This corresponds to an interval of 0.001 non-dimensional time units. This high frequency was used to allow us

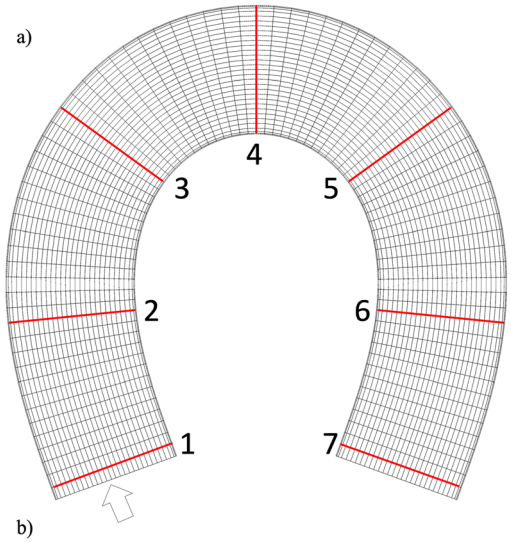

Location	1	2	3	4	5	6	7
x	0.02	0.16	0.35	0.5	0.65	0.84	0.98

FIG. 3. (a) Mesh of measurement probe locations in the n and s directions. Probes are located at every mesh layer in the z direction. The arrow indicates flow direction. The red lines indicate the locations of n–z planes where cross-sectional contour plots will be presented in Secs. VI–VIII of this paper. (b) Locations of n–z planes along s direction. Here, we define an alternative streamwise coordinate $x = 2s/L$.

to undertake spectral analysis on these data in the future. The statistics presented below were calculated based on time averaging performed at the probe locations. The time averaging operator is designated using an overbar (e.g., $\bar{\theta}$), while fluctuating quantities with respect to this mean are denoted with primes (e.g., θ').

V. GENERAL OBSERVATIONS

Figure 4 shows the temperature and vorticity contours on n–s planes at a height of $z = 0.9$ for the neutral (left figures a and c) and stratified (right figures b and d) cases. Top views will be presented at this height throughout this paper. This height was chosen because it captures many of the interesting features associated with secondary flows in the meander, including the outer bank cell. The vorticity field contours show the magnitude of the vorticity vector. For the stratified meander, at the inlet of the bend, the temperature is higher closer to the inner and outer bank. The high temperature at the inner bank gradually diverges from the inner bank and approaches the outer bank as the flow moves nearer to the meander's higher curvature sections. At the same time, the high temperature at the outer bank remains close to the outer bank line for all the channel length. The two high temperature regions converge in the region between locations 3 and 4. (Here, locations can be found in Fig. 3.) This happens due to the formation of two separated shear layers (SSLs) V1 and V2. The first SSL V1 is between the central core of high streamwise velocity fluid and the slowly moving fluid situated close to the inner bank. (Streamwise velocity plots will be shown and discussed in Sec. VI.) The second SSL V2 is located at the outer bank and is introduced to the meander inlet from the meander outlet by the anti-symmetric periodic boundary conditions. The two SSLs can be seen on the temperature contour plot as boundaries between high

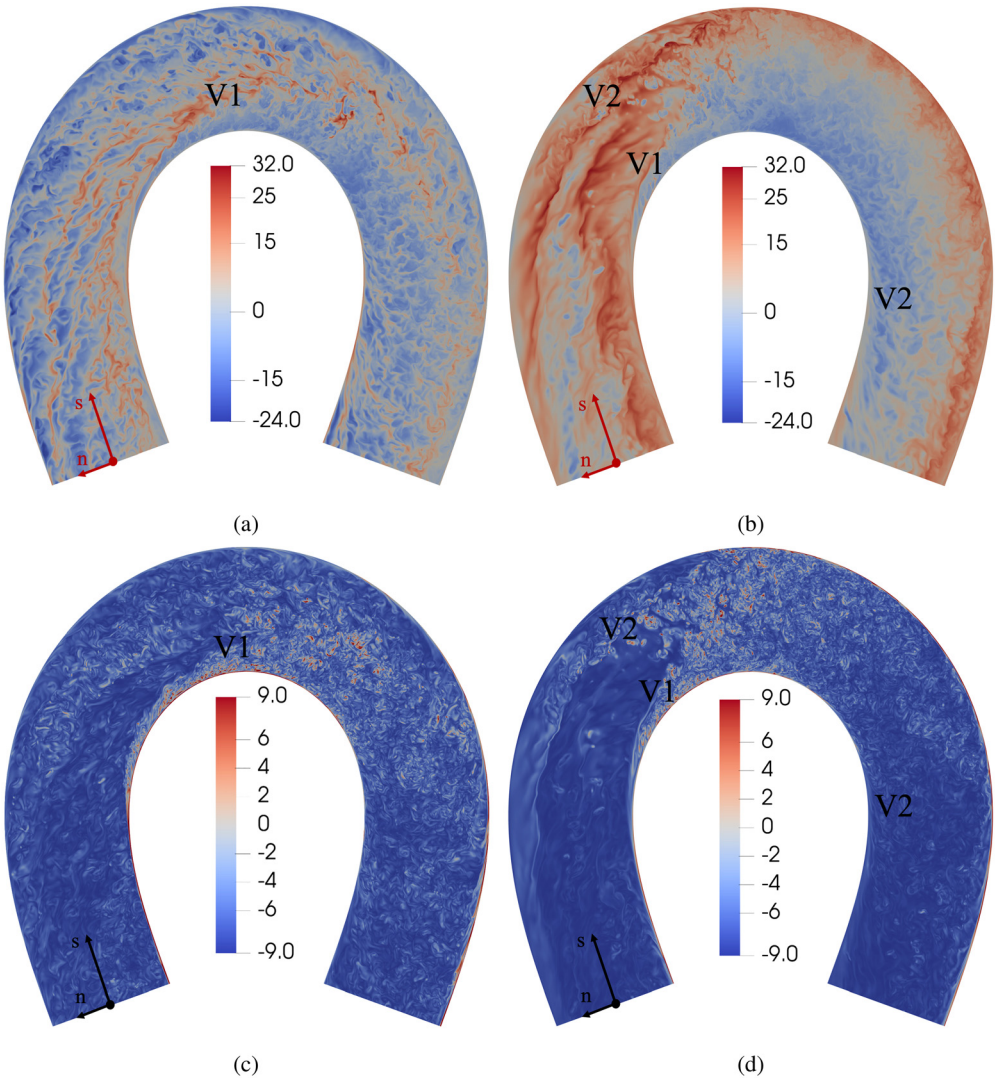

FIG. 4. Contours of instantaneous temperature and vorticity fields on n–s planes at $z = 0.9$. Flow is from left to right. (a) and (b) Temperature field for $\lambda = 0$ and $\lambda = 0.5$ cases. (c) and (d) Vorticity field for $\lambda = 0$ and $\lambda = 0.5$ cases, respectively.

and low temperature regions. In the neutral meander, the SSL V1 is located somewhat further into the bend, closer to the bend apex. Compared with the stratified flow, instead of quickly moving to the outer bank, the high-temperature fluid moves along the middle centerline and does not reach the outer bank until near the outlet. The range of non-dimensional temperatures $\Delta\phi_{max} = 23$ observed is significantly lower than that observed in the thermally stratified case of $\Delta\phi_{max} = 39.5$, indicating that the neutral case allows more mixing. There is a relatively faint presence of SSL V2 for this case. The mechanisms that lead to the formation of these two SSLs V1 and V2 will be discussed in Sec. VI.

The vorticity at $z = 0.9$ is relative weak at the inlet and outlet of both meanders. However, it shows a marked increase at locations 3 and 4 in the range of $x = 0.35$–0.5 for the stratified meander, and further downstream at locations 4 and 5 in the range of $x = 0.5$–0.65 for the neutral case. Turbulence is more strongly amplified in the stratified meander, as this amplification is associated with the passage of the highly energetic eddies generated by the two strong SSLs working together in this region.

VI. MEAN FLOW AND VORTICAL STRUCTURES

The focus of this section is on the mean flow velocities and vortical structures by looking at the contours on both n–z and n–s planes. We use the curvilinear coordinate system with vertical location z, spanwise location n, and streamwise location $x = 2s/L$.

We examine the spatial development of the flow and the lateral circulation of neutral flow ($\lambda = 0$) and stratified flow ($\lambda = 0.5$) in Figs. 5 and 6. Here, time-averaged quantities are plotted.

In Figs. 5(a) and 5(b), visualizations of streamlines generated using spanwise and vertical velocity components show the development of the secondary flow from the inlet at location 1 to outlet at location 7 of the meander. The flow field is characterized by a tricellular pattern of cross-stream motion (v, w) (from inner to outer banks): a small counter-rotating cell occurs near the channel bed inner bank (A), the classical center-region cell (denoted with letter B), and the small outer bank cell (C) observed near the outer sidewall at the surface. Cell (A) becomes cell (A′), cell (B) becomes (B′), and cell (C) can be seen as cell (C′) as the flow moves back from the meander outlet to the inlet by the anti-symmetric periodic boundary conditions.

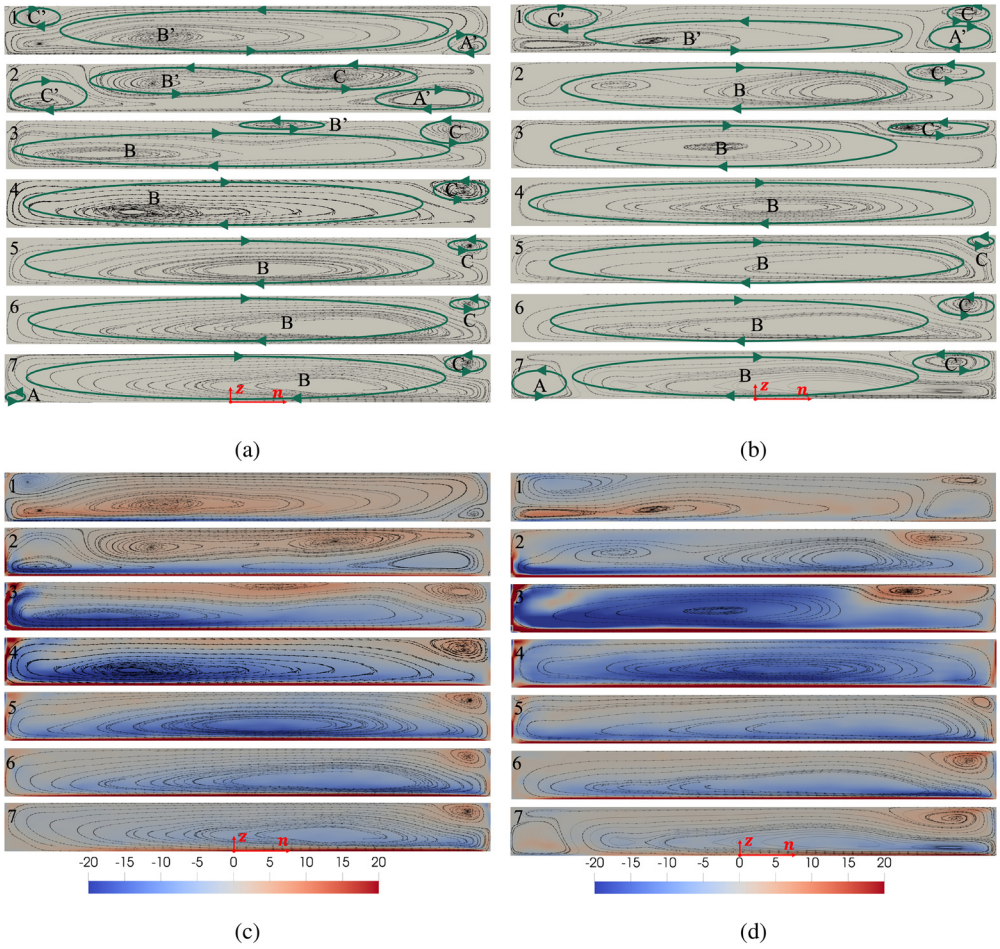

FIG. 5. Contours of the mean flow on n–z planes looking upstream at different locations along the channel. From left to right: inner to outer banks. The non-dimensional streamwise vorticity ω_s is calculated from the mean velocity field and normalized by the steady-state streamwise bulk velocity to depth U_{bulk}/H. (a) and (b) Two dimensional streamline patterns for $\lambda = 0$ and $\lambda = 0.5$ cases. (c) and (d) Streamwise vorticity, $\omega_s H/U_{bulk}$, for $\lambda = 0$ and $\lambda = 0.5$ cases, respectively.

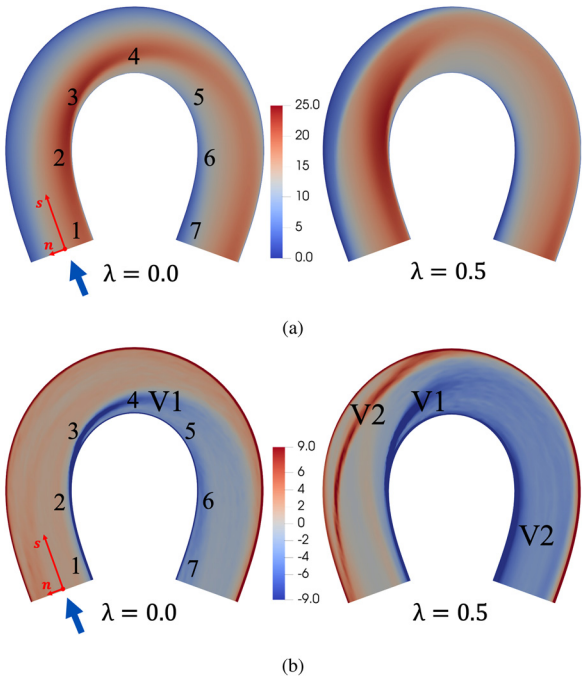

FIG. 6. Contours of the mean flow on $n - s$ planes at $z = 0.9$. Blue arrow indicates direction of the flow. ω_z is normalized by U_{bulk}/H. (a) Streamwise velocity $\bar{u}$ and (b) vertical vorticity $\omega_z H/U_{bulk}$, respectively.

In the neutral case, the outer bank cell (C) appears near location 1 close to the center region of the channel. Here, cell (C) has its maximum size. It reduces size and moves closer to the outer bank at location 3, and the size keeps decreasing as the flow moves downstream before returning through the anti-symmetric periodic boundary to the opposite side of the channel as cell (C′). Cell (C′) can be seen near the channel surface inlet at the inner bank. This cell moves downward as the flow moves near the location 2 region. From there, it expands to almost the whole channel width at location 3, combines with cell (A′), and becomes the central-region cell (B). Cell (B) then stays relatively the same size throughout the rest of the channel.

In the thermally stratified case, the combination of cell (C′) and cell (A′) to form cell (B) happens somewhat earlier near location 1. This makes room for cell (C) to form close to the meander inlet and grows in size as the flow moves toward the apex. It disappears in the region of the apex before reforming at around location 5 and increases in size toward the outlet. The outer bank cell (C) is observed to be largest at the locations between 2 and 3, after which the central region cell (B) expands to the outer bank at the bend apex and suppresses the outer bank cell (C). van Balen *et al.* (2009) showed the development of the outer bank cell to be a result of the interaction between the spatial distribution of turbulent stresses and centrifugal forcing. At the bend apex, where the effect of curvature is the strongest, the strong centrifugal force in the bend drives the fluid in an outward direction at the surface. For the thermally stratified case, reduced mixing due to damping of turbulence by the stable stratification allows the expansion to the outer bank of the center-cell (B). This completely suppresses the outer bank cell (C), and it only appears again when the curvature is reduced after the bend apex. For the neutral case, the center-cell (B) does not expand to the same degree, and the outer bank cell persists through the whole bend.

In both cases, a third small cell [letter A in Figs. 5(a) and 5(b)] is observed near the lower inner bank. This cell becomes cell (A′) at the outer bank inlet due to the anti-symmetric periodic boundary conditions. With the reduction of curvature in this region, there is a reduction in the centrifugal forcing so that the inward spanwise flow near the channel bed is weaker. The reduction in size of the center-region cell (B) makes room for this third circulation cell (A) to be formed at the downstream corner of the inner bank. This phenomenon is reminiscent of corner flow in a lid-driven rectangular cavity (Neary and Stephanoff, 1987) and has not been found in any previous meander flow studies.

In the neutral case, cell (A′) persists until location 2, while in the stratified case, cell (A′) quickly disappears right after the inlet. The disappearance of cell (A′) leaves room at the outer bank for the cell (C) (location 2) to move from close to the centerline to the channel surface near the outer bank (location 3).

The non-dimensional streamwise vorticity ω_s contour can be seen in Figs. 5(c) and 5(d). In both cases, the values of ω_s contour (positive or negative) in the channel correspond with the movements and directions of the three cells. Comparison of the vorticity fields for the neutral and stratified cases show that, from locations 3 to 4 at the meander apex, ω_s is much stronger in the stratified case.

Figure 6 visualizes the mean flow structure on horizontal planes near the free surface at $z = 0.9$. For the neutral case at $z = 0.9$, fluid with high stream-wise velocity is located close to the inner bank from the inlet to the separation point right before the bend apex. The core of inner bank high streamwise momentum fluid tries to preserve its original direction, which is parallel to the direction of the inflow reach. The large bank curvature does not allow the core of high velocity fluid to follow the inner bank, resulting in the high-velocity incoming fluid being deflected away from the inner bank. From there, this high velocity fluid moves gradually outward across the channel and reaches the outer bank near the location 6 (takes approximately 40% the length of the half meander). The associated separated shear layer, V1, is shown Fig. 6(c).

Meanwhile at the same height for the thermally stratified case, the high stream-wise velocity fluid separates from the inner bank somewhat earlier, at around location 3, and quickly approaches the outer bank as the flow moves nearer to the higher curvature section of the meander, responding to the high outward spanwise movement of the flow at the channel surface at the bend apex seen in Fig. 5(b). Here, the high velocity fluid takes only about 15% the length of the half meander to reach the outer bank. The earlier separation from the inner bank and earlier arrival at the outer bank of the high velocity fluid in the thermally stratified case allows the formation of the second separated shear layer, V2, downstream from the bend apex at around location 5, as shown Fig. 6(d). The adverse pressure gradients here are strong enough to allow the wake to continue until it reaches the channel outlet. SSL V2 is transported back through the inlet by the anti-periodic boundary conditions and persists close to the outer bank until just after the bend apex.

In the stratified case, from the meander inlet to location 3, the strong vortical structures associated with the SSL V2 feed into the turbulent kinetic energy and enhance the outer bank cell. Blanckaert and

de Vriend (2004) show that the outer bank cell is enhanced by kinetic energy input from turbulence. This allows the outer bank cell (C) to emerge from the channel inlet, grow, and reach its largest size near the bend apex in the stratified case. For the neutral case, appearing a bit further downstream, turbulence associated with SSL V1 is responsible for the large size of cell (C) in the locations between 3 and 4. However, the absence of the SSL V2 in the neutral case leads to a smaller outer bank cell (C) compared to the thermally stratified case.

For both cases, the formation of a strong SSL V1 between the central core of high streamwise velocity and the slowly moving fluid situated close to the inner bank leads to high shear-driven turbulence production within the shear layer region, as seen in the visualization of the instantaneous vorticity field in Figs. 4(c) and 4(d). (Shear production of turbulence will be discussed in more detail in Sec. VIII.) The SSL V1 penetrates almost to the outer bank for both cases.

In thermally stratified case, from the inlet, SSL V2 moves along the outer bank and interacts with the first SSL (V1). These two SSLs are responsible for a larger amplification of the turbulent kinetic energy (TKE) that is observed from regions near location 3 to the bend apex in the stratified case. The turbulence is amplified more strongly here than in the neutral case in which only one SSL V1 is observed. A possible explanation for the presence of V2 in the stratified case is that stratification might enhance vertical shear, which stretches this SSL far downstream so the anti-symmetric periodic boundary condition can return the SSL (V2) back to the channel inlet. For the case of non-stratified flow through a bend described in Constantinescu *et al.* (2011), a second SSL is also formed behind the bend apex; however, it is not strong enough to stretch to the channel outlet. This is also the case in our study for the neutral flow.

VII. THE TEMPERATURE STRATIFICATION FIELD

Contours of the temperature field for neutral flow ($\lambda = 0$) and stratified flow ($\lambda = 0.5$) are shown in Fig. 7. In general, the cross-stream motions distribute the temperature field in both cases.

In the neutral case, the n–z contour shows a more uniform time mean temperature than that seen in the stratified case. The warmer fluid concentrates at the inner bank before the bend apex and moves to the outer bank downstream after the bend apex.

In the stratified flow in Fig. 7(b), due to thermal stratification, a more complex temperature development is seen. At the channel inlet from locations 1 to 3, the temperature state shows that the channel is weakly stratified in the lower half of the channel and becomes progressively more strongly stratified as the upper surface is approached. Also, at these locations, the interaction of the two counter rotating cells, that is, center-region cell and outer bank cell push the high temperature downward in the region between the two cells [B and C in Fig. 5(b)].

At $Ri_\tau = 10.21$, the flow regime for our stratified flow overall is relatively weakly stratified. However, the bulk internal Froude number $Fr' = 0.39$ [Eq. (16)]. A $Fr' < 1$ here implies a local buoyancy restriction to the development of lateral circulation cells (Nidzieko *et al.*, 2009). As a result, there are regions in the meander where the flow is buoyancy dominated. These regions are predominantly upstream of the bend apex. The degree of temperature stratification decreases as the flow moves through the bend apex. As seen in Fig. 4, there is a significant increase in turbulence close to the upper surface in this part of the flow, which acts to mix the temperature field. At the same time, the high temperature fluid close to the surface is advected toward the outer bank by the central circulation cell. From the bend apex to the outlet, the flow in the channel is divided into two regions with high temperature at the outer bank, and lower temperature at the inner bank following the motion of the central cell. As seen in Fig. 5(a), the central cell spreads out to the outer bank at the bend apex and slowly decreases its size and strength as it continues downstream. As a result, the vertical stratification of the temperature field is gradually restored as the fluid moves toward the outlet and is further heated by the radiative heat source.

For both cases, a region of low temperature is found at the inner bank outlet and outer bank inlet. This is due to the activities of the third counterclockwise cell (A) that keeps the low temperature fluid near the bed.

Figures 7(c) and 7(d) show that the temperature distribution in horizontal planes follows the mean flow movement. For the stratified case, the more complex flow patterns discussed above lead to a more complex temperature field. A significant difference is the formation in the stratified case of a region of high temperature close the outer bank upstream of the bend apex. This region is associated with SSL V2 begins to form along with this SSL close to the inner bank at location 5.

VIII. ANALYSIS OF THE TURBULENCE STRUCTURE

On a non-stratified curved flow, Blanckaert and Graf (2001) reported the distributions of turbulence activity determined from experimental data of the mean velocities and the turbulent stresses. This section will discuss the turbulence characteristics in our sharp stratified meander flow, including the mechanisms underlying the distribution of the TKE, utilizing a term-by-term analysis of the transport equation for TKE. As described in Sec. IV, the equations are solved using physical coordinates on a staggered, orthogonal, curvilinear mesh. In this context, the transport equation for turbulent kinetic energy for a statistically steady-state system can be written as (Richmond *et al.*, 1986)

$$\begin{aligned}
&-\bar{u}(m)\frac{\partial k}{\partial \xi(m)} - \cos\theta_{ij}\overline{u'(j)u'(m)}\nabla(m)\bar{u}(i)\\
&-\overline{u'(m)\frac{\partial}{\partial \xi(m)}\left[\frac{1}{2}\cos\theta_{ij}u'(i)u'(j)\right]}\\
&-\frac{\partial}{\partial \xi(m)}\overline{u'(m)p'} - [D(mm)+\Gamma(nnm)]\overline{u'(m)p'} + \frac{1}{Re_\tau}\nabla^2 k\\
&-\frac{1}{Re_\tau}\cos\theta_{ij}g(mn)\overline{\nabla(m)u'(i)\nabla(n)u'(j)} + \lambda\overline{\phi' u'(3)} = 0.
\end{aligned} \tag{17}$$

Here, k, $\bar{u}$, u', and p' are the turbulent kinetic energy, time mean velocity, velocity fluctuation, and the turbulent pressure fluctuation, respectively. The physical components of the covariant derivative of a contravariant vector Y with respect to coordinate direction ξ^m on an orthogonal mesh are given by

$$\begin{aligned}
\nabla(m)\bar{Y}(i) &= \frac{\partial \bar{Y}(i)}{\partial \xi(m)} + \Gamma(imm)\bar{Y}(m)\\
&= \frac{1}{h_m}\frac{\partial \bar{Y}(i)}{\partial \xi^m} - \frac{1}{h_i h_m}\frac{\partial h_m}{\partial \xi^i}\bar{Y}(m).
\end{aligned} \tag{18}$$

The first three terms on the left-hand side of Eq. (17) are advection A, shear production P, and transport by turbulent fluctuations T. The

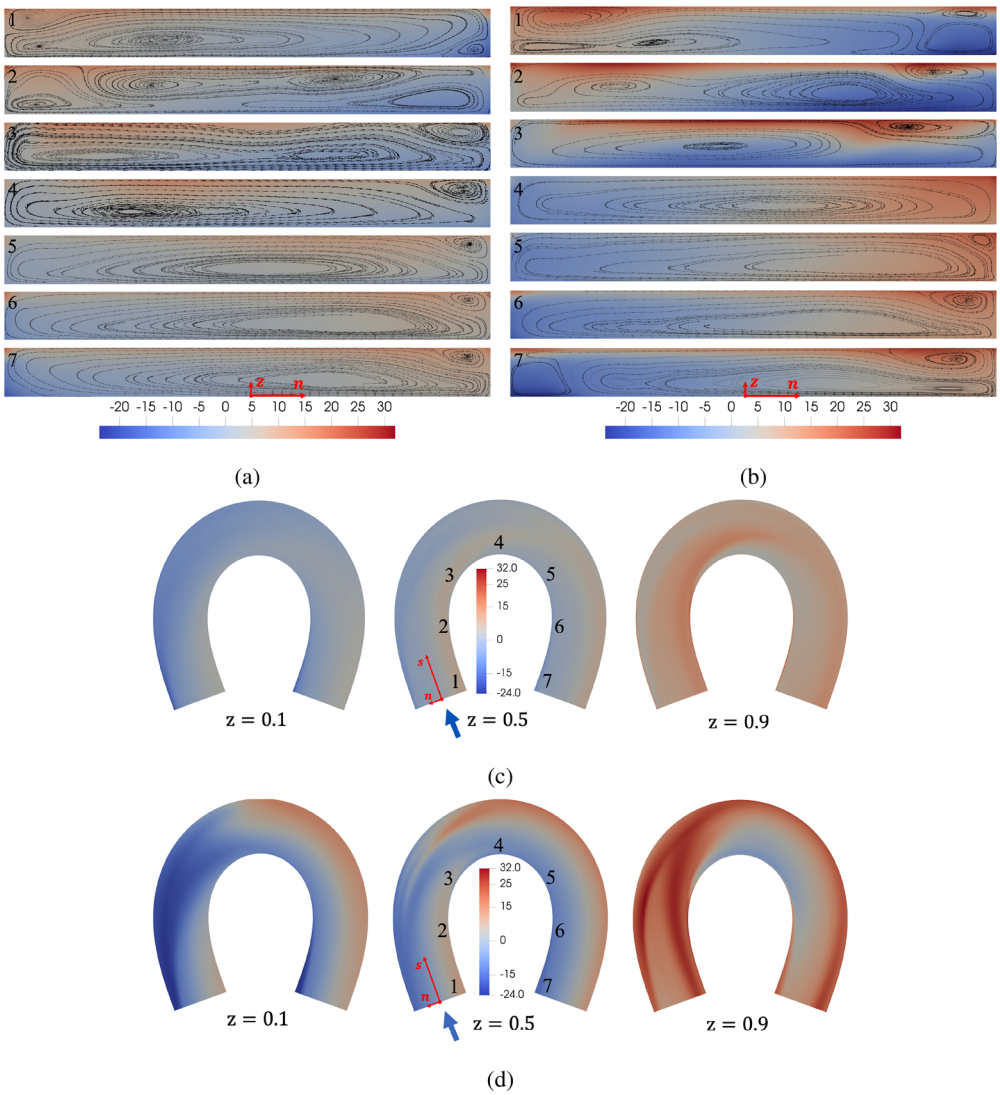

FIG. 7. Contours of time mean temperature $\bar{\phi}$ at different locations along the centerline and at different heights. The negative temperature seen is the result of the scheme used to non-dimensionalize the equations. (a) and (b) *n*–*z* contour for $\lambda = 0$ and $\lambda = 0.5$ cases. (c) and (d) *n*–*s* contour for $\lambda = 0$ and $\lambda = 0.5$ cases, respectively.

next two terms combined represent turbulent diffusion due to pressure fluctuations. The last two terms are dissipation rate ε and buoyancy destruction B, respectively. Here, $\Gamma(imm)$ are physical components of Christoffel symbols, h_m is the scale factor, and $\xi(m)$ is a curvilinear coordinate. We use the following notation conventions. An index within parentheses, for example (m), indicates the physical component of a vector, a superscript index indicates the contravariant components of a vector, and a subscripted index indicates covariant components. In an orthogonal coordinate system,

$$\Gamma(imm) = \frac{h_i}{h_m h_m}\Gamma^i_{mm} = -\frac{1}{h_i h_m}\frac{\partial h_m}{\partial \xi^m}, \tag{19}$$

$$D(mm) = -\Gamma(mmm) = -\frac{1}{h_m^2}\frac{\partial h_m}{\partial \xi^m}. \tag{20}$$

The direction cosines are as follows:

$$\begin{aligned} \cos\theta_{ij} &= 1 \quad \text{for } i = j, \\ \cos\theta_{ij} &= 0 \quad \text{for } i \neq j, \end{aligned} \tag{21}$$

and the physical components of the metric tensor,

$$\begin{aligned} g(mn) &= \frac{g_{mm}}{h_m h_m} = 1 \quad \text{for } m = n, \\ g(mn) &= 0 \qquad\qquad \text{for } m \neq n. \end{aligned} \tag{22}$$

This leads to simplification of the terms in Eq. (17). We will focus on the dominant terms as follows:

Advection A,

$$A = -\bar{u}(m)\frac{\partial k}{\partial \xi(m)}. \tag{23}$$

Shear production P,

$$P = -\cos\theta_{ij}\overline{u'(j)u'(m)}\nabla(m)\bar{u}(i) = -\overline{u'(i)u'(m)}\nabla(m)\bar{u}(i). \tag{24}$$

Transport by turbulent fluctuations T,

$$T = -\overline{u'(m)\frac{\partial}{\partial \xi(m)}\left[\frac{1}{2}\cos\theta_{ij}u'(i)u'(j)\right]}$$

$$= -\frac{1}{2}\overline{u'(m)\frac{\partial(u'(i)u'(i))}{\partial \xi(m)}}. \tag{25}$$

Dissipation rate ε,

$$\varepsilon = \frac{1}{Re_\tau}\cos\theta_{ij}g(mn)\overline{\nabla(m)u'(i)\nabla(n)u'(j)}$$

$$= \frac{1}{Re_\tau}\overline{\nabla(m)u'(i)\nabla(m)u'(i)}. \tag{26}$$

The downward buoyancy flux (or buoyancy destruction) B,

$$B = -\lambda\overline{\phi' w'}. \tag{27}$$

We refer the interested reader to (Aris, 1990) for theoretical background that leads to the derivation of the terms given in Eqs. (18)–(26). All the covariant derivatives were computed using second-order central differences. The Christoffel symbols and the scale factors were computed analytically.

Figures 8 and 9 show the normalized contour distributions of the mean-flow kinetic energy K and the turbulent kinetic energy k, in n–z and n–s planes, respectively, in which K and k are defined as

$$K = \frac{1}{2}(\bar{u}^2 + \bar{v}^2 + \bar{w}^2); \quad k = \frac{1}{2}(\overline{u'^2} + \overline{v'^2} + \overline{w'^2}), \tag{28}$$

and K and k are shown normalized by $\frac{1}{2}U_{bulk}^2$.

The distributions of K and k show complex behavior. Because the streamwise velocity component is dominant, contours of K in Fig. 8(a) for neutral flow and in Fig. 8(b) for stratified flow show similar

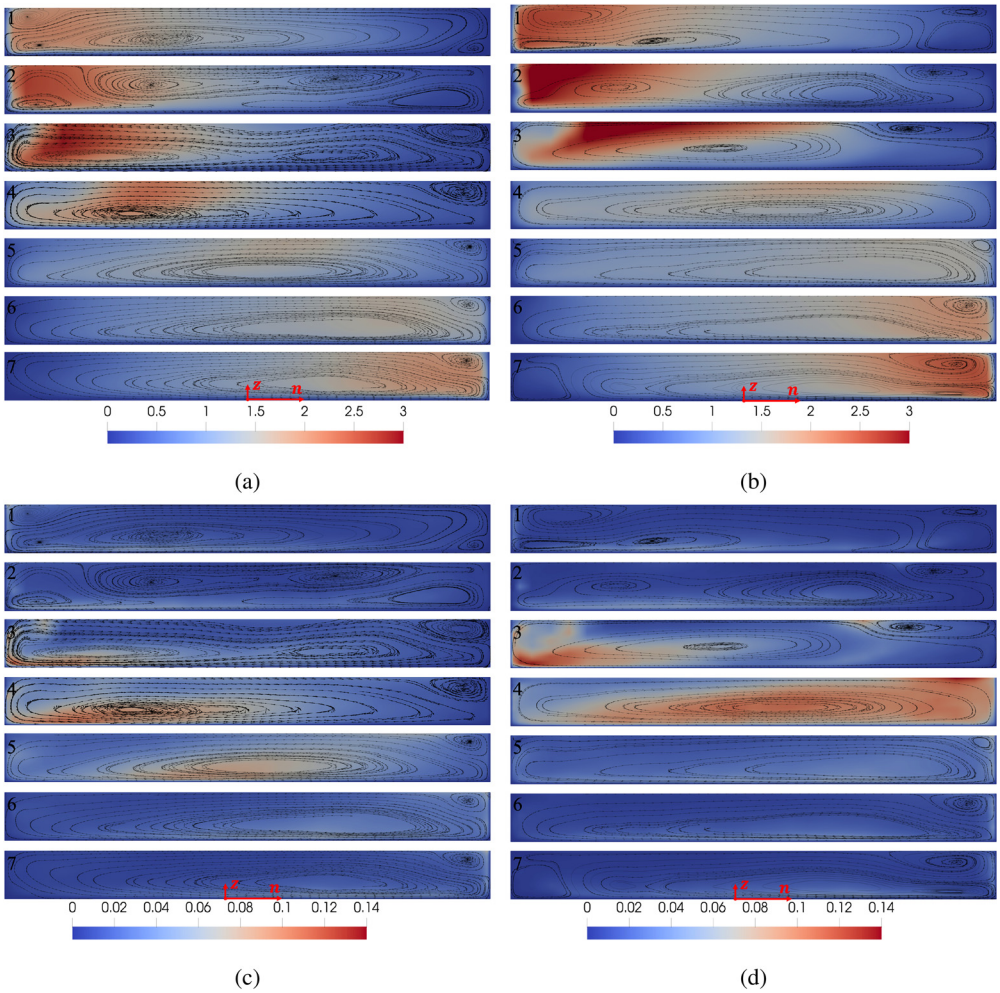

FIG. 8. (a) and (b) Contours of $K/(\frac{1}{2}U_{bulk}^2)$ for $\lambda = 0$ and $\lambda = 0.5$ cases. (c) and (d) $k/(\frac{1}{2}U_{bulk}^2)$ for $\lambda = 0$ and $\lambda = 0.5$, respectively, on n–z planes looking upstream at different locations along the centerline. From left to right: inner to outer banks.

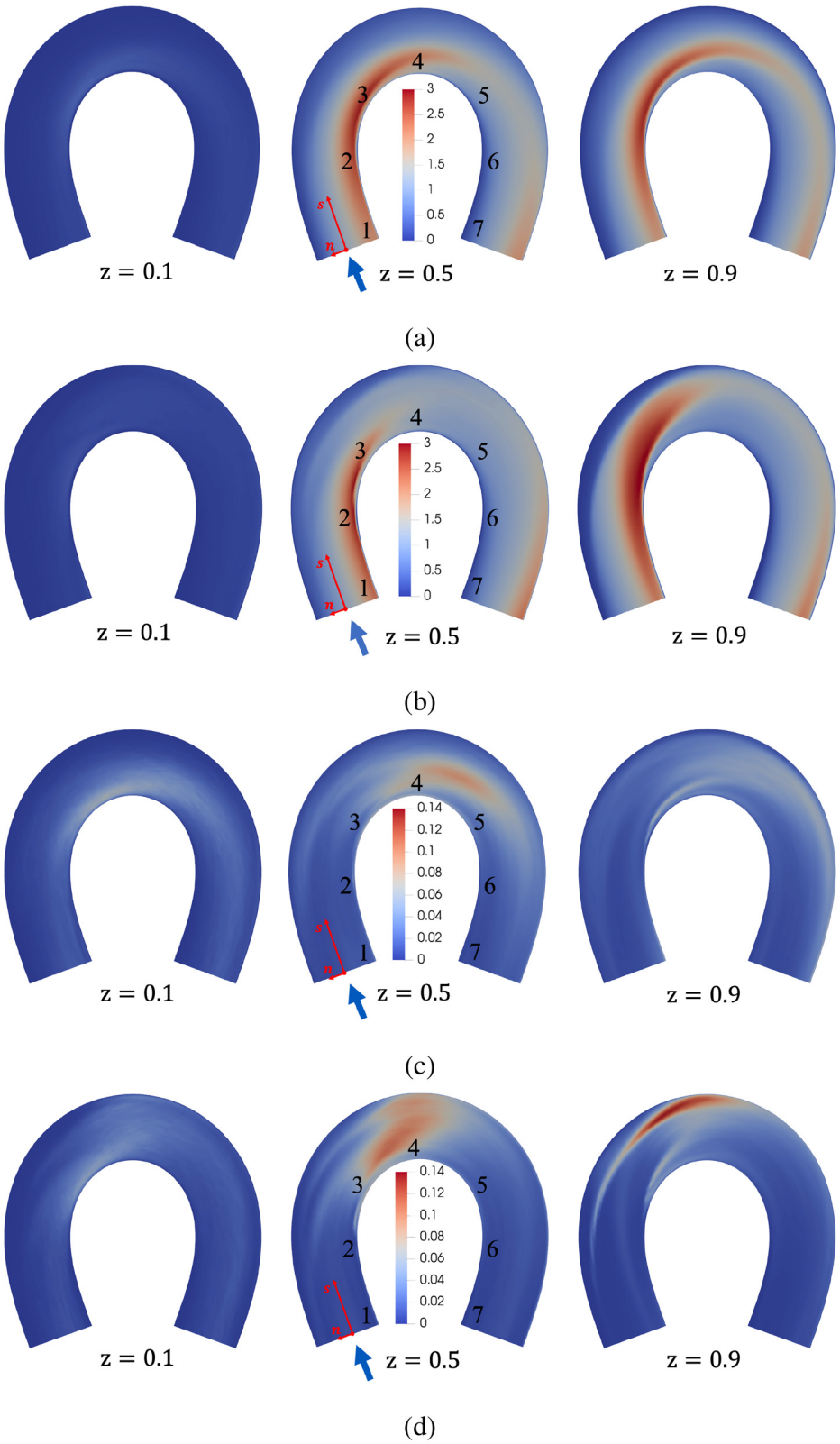

FIG. 9. (a) and (b) Contours of $K/(\frac{1}{2}U_{bulk}^2)$ for $\lambda = 0$ and $\lambda = 0.5$ cases. (c) and (d) $k/(\frac{1}{2}U_{bulk}^2)$ for $\lambda = 0$ and $\lambda = 0.5$ cases, respectively, on n–s planes at $z = 0.1$, 0.5, and 0.9. Blue arrow indicates direction of the flow.

characteristics to those of their mean streamwise velocity, respectively. As in Fig. 5, near the meander inlet K is concentrated close to the inner bank as a result of passing through the previously inverted meander bend. In the stratified case, from approximately locations 3 to 4 near the meander apex, K is transported toward the outer bank across the surface of the channel by the central secondary flow cell. At the meander apex, K spreads out evenly through the whole cross section, with a little higher value at the surface at the channel centerline. K distribution here is aligned with the center-region cell's cross-stream motion at the bend apex, which covers the whole channel width. As the flow approaches the exit of the meander, this circulation continues and K becomes concentrated close to the outer bank. In the neutral case, the region of high K is more restricted and reaches the outer bank later due to weaker advection across the surface in the region of the bend apex by the central circulation cell. At the meander apex, high K still concentrates at the inner bank and only moves to the middle of the channel at location 5 after the bend apex.

The third counterclockwise cell that develops in the lower part of the channel close to the inner bank in the wake after the bend apex [see regions with letter A in Figs. 5(a) and 5(b)] is consistent with the low value of K in the outer bank at the inlet and inner bank at the outlet, as seen in Figs. 8(a) and 8(b) and 9(a) and 9(b). Close to the inner bank outlet, the counterclockwise rotation of the third circulation cell (A) pushes the center-region cell's high-velocity patches closer to the centerline, which moves the high K location outward. Interactions between the third bank cell and the center-region cell give an approximately anti-symmetric distribution of K with respect to the bend apex, that is, higher K concentrates near the inner bank at the inlet and near the outer bank at the outlet. This is different from the K distribution with the single bend non-stratified flow presented by Blanckaert and de Vriend (2005b), where K is maximum at the lower part of the water column at the separation between the center-region and outer bank cells. As described in Sec. VI, the mean flow patterns in the single bend flow are different from our meander case with the anti-symmetric periodic boundary conditions. This difference leads to the difference in K distribution.

The distribution of k is shown in Figs. 8(c) and 8(d) and 9(c) and 9(d) for both cases. At the inlet, close to the inner bank k has relatively low values over the width. From location 3 to the meander apex, for both cases, the high k values close to the bed are concentrated near the inner bank. For the stratified case, there is also a small region of high k at the surface at the same location as the outer bank cell. This coincides with the development of the two SSLs (V1 and V2) at this location seen in Fig. 6(b). For neutral flow, k increases as the flow moves through the bend apex. The SSL V1 extends to the middle of the channel and amplifies k here. This amplification continues through the bend apex until location 5. For the thermally stratified case, we observe a much stronger turbulence amplification. As the two SSLs increase their strength and size, at the bend apex at location 4, k is energetically amplified, and high values of k extend across the whole channel width. Moving past the meander apex, k gradually decreases.

It is interesting to note that, similar to the findings of Blanckaert and de Vriend (2005b) for non-stratified flow, the high values of k approximately coincide with regions containing low values of K. However, at the location of the third counterclockwise cell [regions with letter A in Fig. 5(a)], we observe a low value for both k and K. Additionally, for the stratified case, adjacent to the bend apex, the activity of the second SSL (V2) at the outer bank increases the turbulent kinetic energy there, which is different from the non-stratified single bend case of Blanckaert and de Vriend (2005b) and our neutral case, where a reduction of turbulence activity in the outer bend is observed.

To gain insight into the mechanisms underlying the k distribution, we look at terms of Eq. (17) that, in our steady-state flow, correspond to the sources, sinks and transport of local k. Contours of P, ϵ, B, A, and T, are shown in Figs. 10, 11, 12, 14, and 15, respectively. Here, in order to maintain clarity, we present results of the stratified flow case only. Similar arguments apply to the neutral flow case.

In Fig. 10, contours of shear production P from Eq. (24) are shown. P represents the exchange energy of kinetic energy between mean flow and turbulence, which occurs through the work of deformation of the mean motion by turbulent stresses.

Due to the bed friction, P is higher near the bed over the whole width of the flow. Close to the surface, high values of P are found at the location of the outer bank cell near the meander apex. The magnitude of P in the outer bank region is more profound than that in the center region. The outer bank cell might enhance P and the long stretch of the second SSL is responsible for the high level of shear stress at this location. High positive P occurs where there is high shear and high turbulent stresses. This occurs within the SSLs, which are visualized by the region of high ω_z. It can be seen that a high positive P at

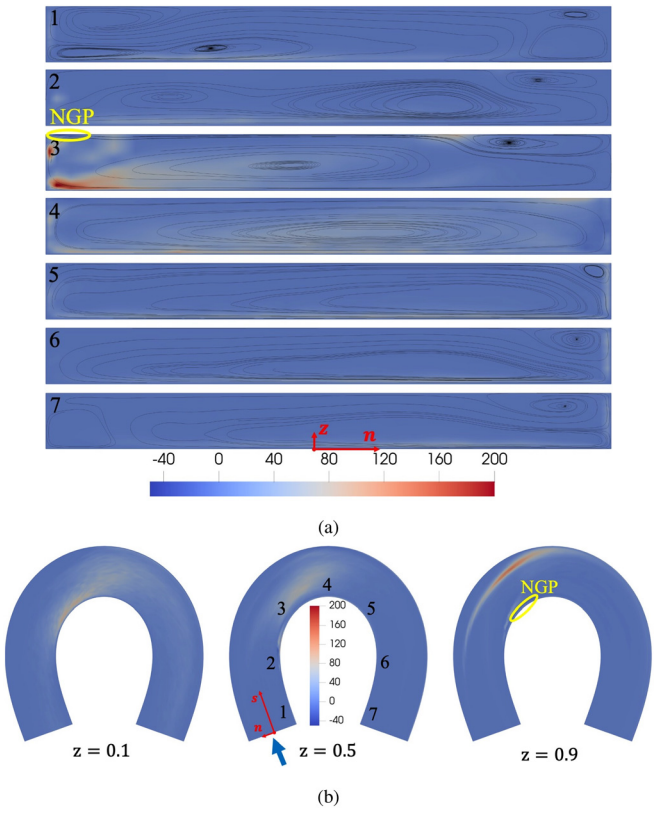

FIG. 10. Contours of shear production P at different locations along the centerline and at different heights ($\lambda = 0.5$). (a) n–z contour and (b) n–s contour.

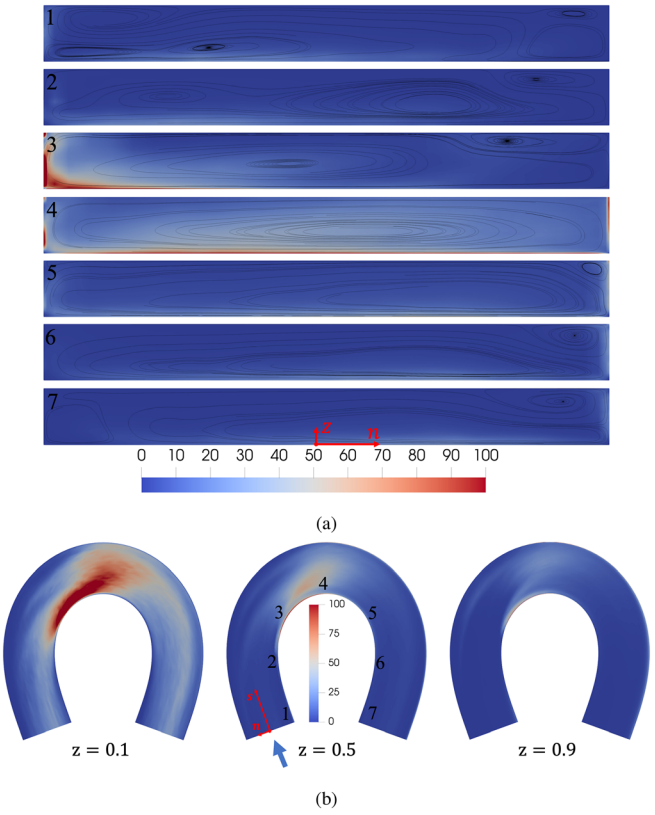

FIG. 11. Contours of dissipation rate ϵ at different locations along the centerline and at different heights ($\lambda = 0.5$). (a) *n*–*z* contour and (b) *n*–*s* contour.

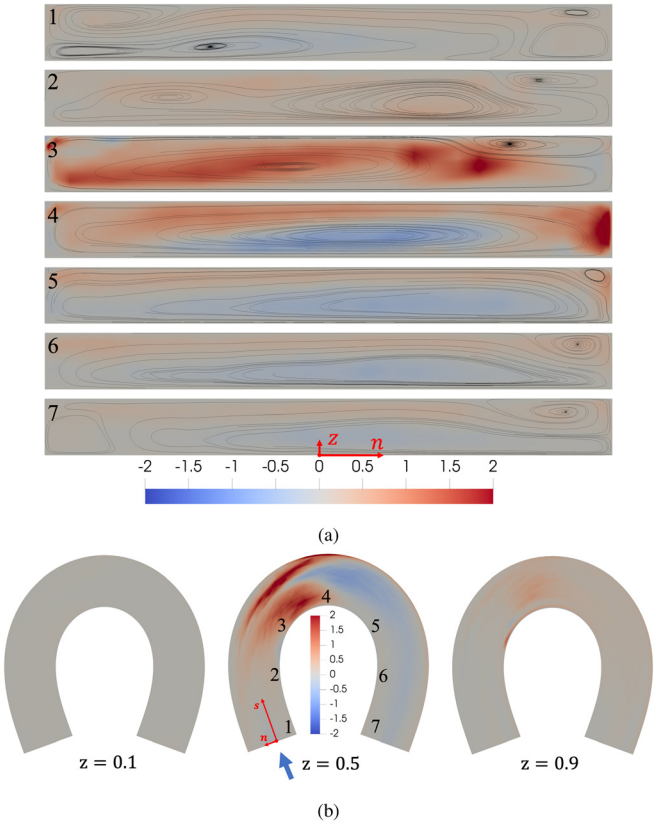

FIG. 12. Contours of downward turbulent buoyancy flux *B* at different locations along the centerline and at different heights ($\lambda = 0.5$). (a) *n*–*z* contour and (b) *n*–*s* contour.

$z = 0.9$ in Fig. 10(b) corresponds to the location of SSLs V1 and V2 at $z = 0.9$ in Fig. 6(b).

Zones with $P < 0$ tend to reduce k and vice versa, $P > 0$ drives an increase in k. P contours, therefore, have a similar behavior as k contours in Figs. 8 and 9. At location 3, the high P is concentrated near the inner bend. This is a region of turbulent amplification. The strong activity of the two SSLs generate strong shear in this region. k is also high at this location. Also, at location 3 close to the surface outer bank, there is a small region of high P and k, which results from the shear generated by the outer bank cell. The strength and size of the two SSLs are maximal at the bend apex, which in turn gives highly positive shear production P, and leads to high production of k through the whole channel width at the bend apex. P stays positive for most of the channel; however, a small region of $P < 0$ can be found near the inner bank surface (the region is noted as negative P—NGP in Fig. 10). An explanation of this will be given below when shear stresses are presented. The result is in contrast with the single bend unstratified channel flow study by Blanckaert and de Vriend (2005a), where negative values of P are observed over most of the flow depth in a region close to the inner bank.

Although a negative contribution may exist in some regions of the flow domain, the sum of P is globally positive and is a net source of k production. Globally speaking, P is balanced with $B + \varepsilon$, but locally, P and $B + \varepsilon$ may not balance due to transport terms, predominantly A and T.

The dissipation rate ε, a sink term in the TKE equation, is shown in Fig. 11. Turbulent kinetic energy is converted into internal energy through viscous dissipation ε. From Fig. 11, turbulent dissipation rate ε is higher near the bed throughout the channel. At the location 3, there is an amplification of ε near the bed close to the inner bank. Here, the strong viscous shear stresses, that are associated with the strong activity of the SSL (V1), perform deformation work which increases the internal energy of the fluid at the expense of the turbulent kinetic energy, which increases the rate of turbulent dissipation.

Contours of downward turbulent buoyancy flux B are shown in Fig. 12. In general, B has a small order of magnitude ($-2 < B < 2$) compared to other terms in the TKE equation. This is due to the relatively low value of the buoyancy coefficient $\lambda = 0.5$ and a small friction Richardson number $Ri_\tau = 10.21$, and hence relatively weak stratification.

Positive downward buoyancy flux acts as a sink term in the turbulent kinetic energy budget. In Fig. 12, B has higher values in the upper part of the channel. The buoyancy flux here is downward ($B > 0$), indicating a net transfer of energy from turbulent kinetic energy to potential energy (buoyancy destruction). In the lower part of the channel, the buoyancy flux is upward ($B < 0$), indicating a net transfer of energy from potential energy to turbulent kinetic energy (buoyancy production).

We find high and positive B in the regions of a high vertical temperature gradient. Figure 7 shows that there is a high vertical temperature gradient at the region between the center-region cell and outer bank cell at location 3, and at the outer bank at the bend apex. Those regions also show high positive B.

As the flow moves toward the higher curvature region, the net downward turbulent heat flux moves down from the channel surface, and is strongly enhanced at the region where the turbulence generated by the two SSLs breaks down stratification at location 3. There is a thick layer of positive B in the middle of the channel and negative B close to the top and bottom. The vertical profile of B at location 3 has a typical convex shape (high value in the middle and low values at the top and the bottom) seen in stably stratified turbulent boundary layers that contain a thermocline, including thermally stratified open channel flow in a straight channel [see, e.g., Williamson *et al.* (2015); Kirkpatrick *et al.* (2019)].

At the bend apex, the turbulent heat flux changes values when the temperature gradient decreases rapidly. The upward heat flux is magnified, which creates a region of negative B in the middle of the channel. This patch of negative B decreases as the fluid moves downstream.

Contours of the streamwise–spanwise $\overline{u'v'}$ and streamwise–vertical $\overline{u'w'}$ stresses for different locations along the centerline are shown in Figs. 13(a) and 13(b), respectively. The two shear stresses are induced by cross-sectional gradients in the streamwise velocity interacting with the lateral circulations. The maxima and minima of the two turbulent shear stresses are of similar magnitude, with a slightly smaller magnitude for $\overline{u'w'}$. At the locations of turbulence amplification, locations 3 and 4, $\overline{u'w'}$ reaches high values near the shear layer at the edge of the zone of convex bank flow separation [region A in Fig. 13(b)] where the flow is characterized by pronounced positive values of $\overline{u'w'}$ in the upper half of the channel and pronounced negative values in the lower half of the channel. This is aligned with findings of Blanckaert (2015). At locations 3 and 4, high $\overline{u'v'}$ is concentrated near the inner bank (region A) and at the location of the outer bank cells (regions B and C). A similar region of high $\overline{u'v'}$ stress values was also observed in the measurements of Booij (2003) and the computations of van Balen *et al.* (2009) and van Balen *et al.* (2010) of curved open channel flow. Those are also locations of the two separated shear layers V1 and V2.

The n–s contours of $\overline{u'v'}$ are given in Fig. 13(c). The high turbulent stress $\overline{u'v'}$ regions in Fig. 13(c) are in the same locations of SSLs V1 and V2 [Fig. 6(b)].

Contours of dominant components of shear production P are shown in Fig. 13(d). Together, those components can give a prediction of turbulent production distribution. Cimarelli *et al.* (2019) noted that for a 2D flow with leading edge separation, negative shear of production takes origin from a positive relation of vertical and streamwise shear with the Reynolds stresses $\overline{u'v'}\frac{\overline{du}}{dy} + \overline{u'v'}\frac{\overline{dv}}{dx} > 0$, while Blanckaert and de Vriend (2005a) found a region of negative production near the bottom of the inner bank for flow through a sharp bend. They argue that the positive value of $\overline{u'w'}\frac{\overline{du}}{dz}$ at that region is the reason for $P < 0$. In our flow, regions of positive $\overline{u'v'}\frac{\overline{du}}{dy}$ and positive $\overline{u'w'}\frac{\overline{du}}{dz}$, which overcome the negative contribution of $\overline{u'v'}\frac{\overline{dv}}{dx}$ to the turbulent production can be found at the location of negative P [labeled NGP on Figs. 10 and 13(d)].

Contours of the turbulent advection term A are presented in Fig. 14. A represents the convection of TKE by the mean motion of the fluid from one location to another in the channel. In the Eulerian viewpoint, A represents the net advective flux of k into an small region in space.

In general, A has a higher magnitude relative to other terms in the TKE budget. A is negative everywhere, indicating that the flux is always outward. In general, A can be seen to transport TKE away from regions where it is strongly produced. At location 3 where the two SSLs meet, shear production P is high, which produces strong TKE, leading to highly negative A in this region.

Transport of k by turbulent fluctuations is calculated using Eq. (25) and is shown in Fig. 15. T is responsible for the redistribution of k in the channel in which T transports k out of regions of high P. T is also important to maintain the TKE budget in the regions where the buoyancy destruction B of the TKE is large, where the TKE is spent to work against the gravity. In Fig. 15, T generally has high values near the bed. The negative T matches regions of high P, as can clearly be seen with a stretch of high positive P at $z = 0.9$ [Fig. 10(b)] that corresponds to the stretch of negative T in the same region [Fig. 15(b)].

Combined with A, T provides most of the local transport of TKE in and out of small regions.

To understand more of the relation between k and P, we will take a closer look at the turbulence structure parameter a_1. Similar analysis has been undertaken previously by Blanckaert and de Vriend (2005a) for a curved non-stratified flow.

The turbulence–structure parameter a_1 is defined by Schwarz and Bradshaw (1994) as

$$a_1 = \frac{\sqrt{\overline{u'w'}^2 + \overline{v'w'}^2}}{2k}. \tag{29}$$

The a_1 parameter can be crudely regarded as the efficiency of eddies in producing turbulent shear stresses for a given amount of turbulent kinetic energy. An increase in a_1 is accompanied by increases in turbulent shear stress and vice versa. A contour plot of a_1 is shown in Fig. 16.

As can be seen in Fig. 16, high values of a_1 can be found in the central parts of the center-region cells (B). This indicates that the streamwise–vertical and spanwise–vertical Reynolds stresses clearly correlate with the large scale circulation structures that occur in the channel cross section. This has also been observed for straight and curved non-stratified open-channel flows (Blanckaert and de Vriend, 2005a; van Balen *et al.*, 2010).

The turbulence–structure parameter a_l correlates quite closely with P. The a_1 parameter values are lower near the channel surface, in response to low values of P in the adjacent regions. The high values of a_1 near the inner bend, especially at our focused locations 3 and 5, correspond consistently with regions of high P.

IX. DISCUSSION AND CONCLUSIONS

This paper presented a DNS study on a high-resolution curvilinear mesh of neutral and thermally stratified open-channel flow through a sharp periodic meander at $Re_\tau = 200$. We have described the structure of the mean flow for both cases, as well as interactions between the dominant terms in the turbulence kinetic energy budget for the stratified case. This study fills a gap in the literature with respect to turbulence activity in meandering stratified open-channel flow.

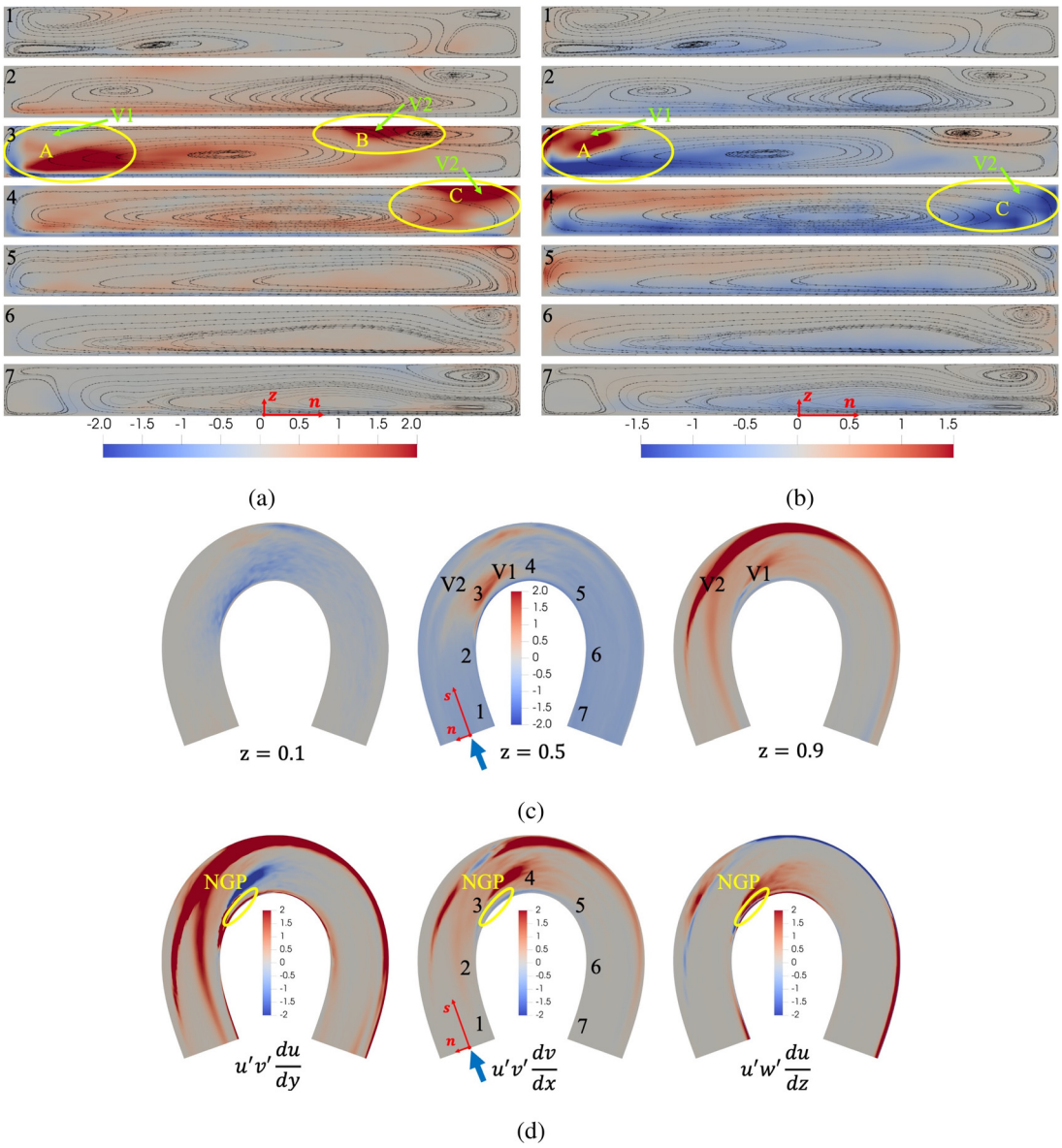

FIG. 13. (a) and (c) Contours of turbulent stresses $\overline{u'v'}$ on n–z and n–s planes, respectively. (b) Contours of $\overline{u'w'}$ on n–z planes and (d) components of shear production P: $\overline{u'v'}\frac{du}{dy}$, $\overline{u'v'}\frac{dv}{dx}$, and $\overline{u'w'}\frac{du}{dz}$ on n–s planes, at different locations along the centerline and at different heights ($\lambda = 0.5$).

Compared to non-stratified single bend flow with bi-cellular circulation cells, that is, a classical center-region cell and an outer bank cell, in our meander study we identify a third cell close to the bed at the inner bank outlet and outer bank inlet for both the neutral and stratified cases. The three cells can be observed in Figs. 5(a) and 5(b), denoted as B, C, and A, respectively. The cross-stream motions associated with the three cells and their interaction with the streamwise velocity determine both the mean and turbulent structure of the flow.

The development of the small cells (A and C) depends on the strength and size of the central cell (B). In the stratified case, close to the bend apex, where the curvature is highest so that the driving centrifugal force is strongest, the center-region cell spreads out over the whole channel width and suppresses the outer bank cell. The outer bank cell only appears again after the bend apex when the curvature decreases. For the neutral case, the absence of stable stratification leads to more turbulent mixing which reduces the extent of this cell. As a result, the outer bank cell (C) persists through the bend.

For both cases, the flow separates from the inner bank upstream of the bend apex near location 3. From there, near the inner bank, the high velocity fluid moves outward to the outer bank as the flow moves

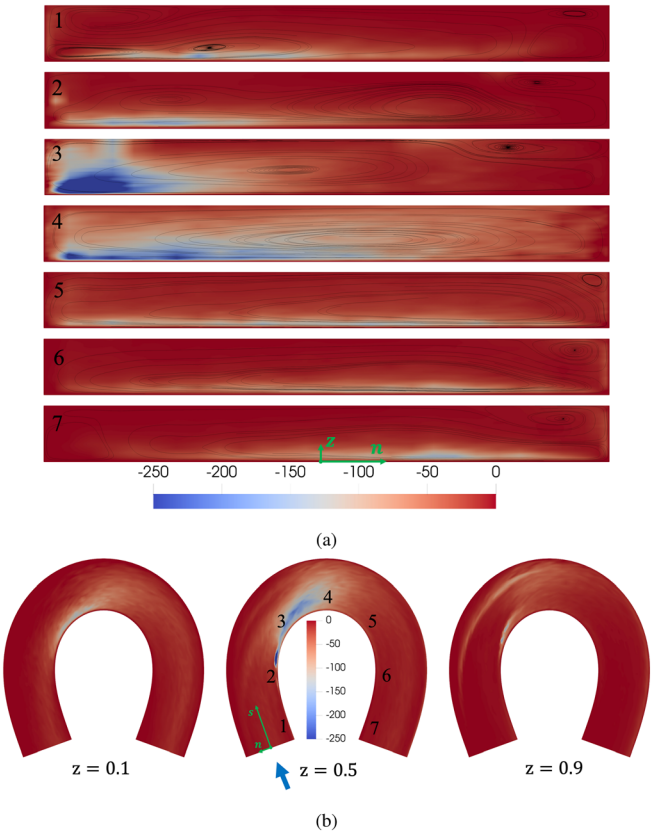

FIG. 14. Contours of advection A at different locations along the centerline and at different heights ($\lambda = 0.5$). (a) n–z contour and (b) n–s contour.

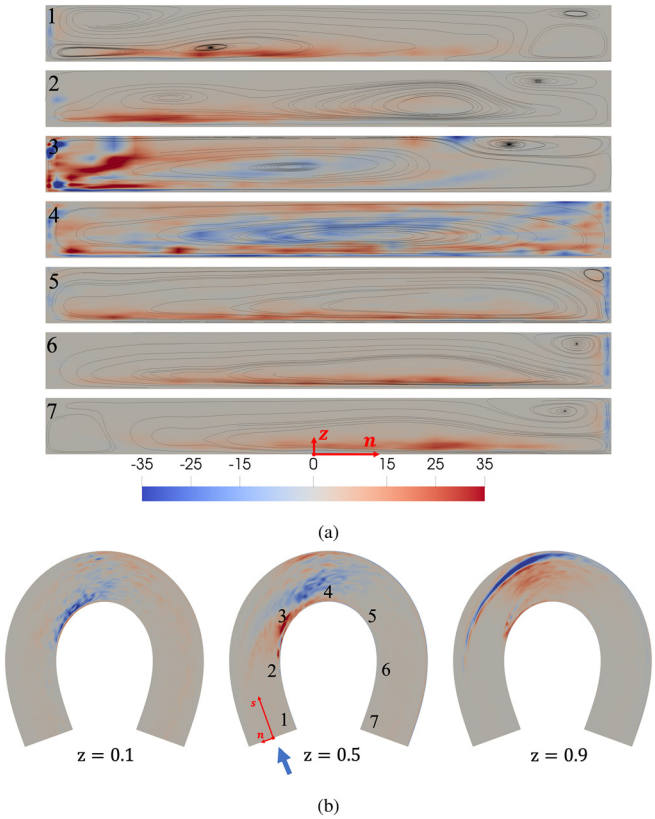

FIG. 15. Contours of transport due to turbulent fluctuation T at different locations along the centerline and at different heights ($\lambda = 0.5$). (a) n–z contour and (b) n–s contour.

closer to the high curvature region. The high curvature forces the flow to separate as the high streamwise momentum fluid tries to preserve its original direction. This leads to a separated shear layer, which we have denoted V1. The stronger central circulation cell (B) for the stratified case causes this SSL to traverse the channel more rapidly than for the neutral flow, which results in a larger wake region for the stratified flow. This enables the generation of a second SSL, V2, downstream of the bend apex at location 5 for this case. SSL stretches until the outlet, is then introduced back to the meander inlet by the anti-symmetric periodic boundary conditions, and then continues along the meander outer bank. This second SSL is not observed in the neutral case.

Similar flow morphology has also been observed in higher Reynolds number flows, including an LES study of Kashyap *et al.* (2010) and a DES study by Constantinescu *et al.* (2011) on neutral flows through channel bends with rectangular cross sections and deformed beds. Those studies also note the formation of SSLs in the inner bank separation zones. The Reynolds numbers in those studies are much higher than in our simulation (e.g., $Re_b = 68\,400$, compared to our simulation for which $Re_b = 2700$). Nonetheless, they also found SSL patches forming in a similar inner bank region.

For both neutral and stratified cases, we observed a marked increase in TKE close to the bend apex. Turbulence amplification is a characteristic feature of flows with strong inner bank curvatures. SSL V1 induces a region of high vorticity and shears that feed shear

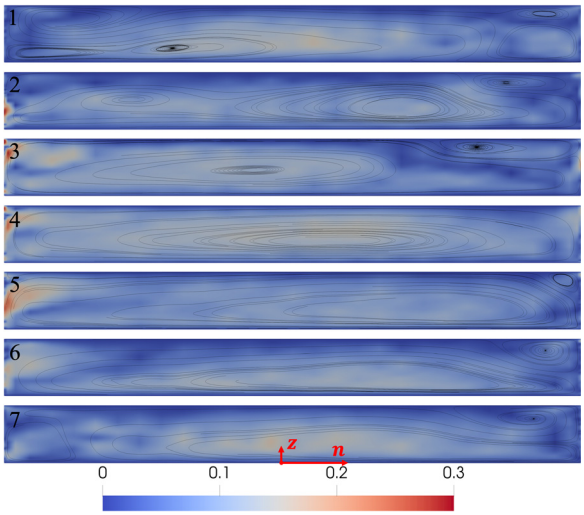

FIG. 16. Contours of the value of turbulence-structure parameter a_1 on n–z planes looking upstream at different locations along the centerline. From left to right: inner to outer banks ($\lambda = 0.5$).

production and hence amplifies the TKE. For the stratified case, the production of TKE is further enhanced by the presence of the second SSL, V2. Compared to the neutral case, SSLs V1 and V2 converge in the region before the bend apex and amplify the turbulence more strongly there. SSL V2 activity also enhances TKE close to the outer bank near the meander apex, while there is no such observation in our neutral case, or in other studies of neutral flow through a single bend.

The temperature field follows the cross-stream motions. It is distributed more uniformly in the neutral case. Fluid heated by the radiative heat source in the region close to the upper surface and cooler fluid from close to the channel bed are advected by the complex tricellular circulation structure. The larger center-region cell plays a dominant role in determining the temperature distribution over most of the channel; however, the two smaller cells have noticeable effects in near bank regions.

An analysis of the distribution mechanism of turbulent kinetic energy k was made via term-by-term evaluation of the TKE transport equation, with attention given to terms representing the production P, dissipation ε, buoyancy flux B, advective transport A, and turbulent transport T of k. These latter two mechanisms transport k out of regions of high production P and, hence, redistribute k in the channel. The dominant terms with larger magnitude in our flow are A, P, and ε. There is a rather weak correlation between the dissipation rate ε and k; however, a strong correlation between the shear production P and k is found. P dominates the distribution of k in our stratified case. A combination of advection by the cross-stream circulation cells and turbulent buoyancy flux B act to break down the temperature stratification as the flow moves into the high curvature region.

Turbulent kinetic energy k is found to be quite high close to the outer bank in the region before the meander apex. This feature has not been observed in studies of neutral flow through a single bend and appears to be due to the periodic nature of our meandering flow. The strong enhancement of k at these locations feeds into the strong development of the outer bank cells.

ACKNOWLEDGMENTS

The authors gratefully acknowledge the support of the Australian Research Council (ARC). The research in this paper was supported by ARC Discovery Project No. DP150100912. The authors also acknowledge the National Computational Infrastructure (NCI), which is supported by the Australian Government and its high-performance computing facility, Gadi, which was used to run the simulations, and the Sydney Informatics Hub supercomputer Artemis and Orc cluster at the University of Sydney, which were used for post-processing calculations.

AUTHOR DECLARATIONS

Conflict of Interest

The authors have no conflicts to disclose.

DATA AVAILABILITY

The data that support the findings of this study are available from the corresponding author upon reasonable request.

REFERENCES

Aris, R., *Vectors, Tensors and the Basic Equations of Fluid Mechanics*, Dover Books on Mathematics (Dover Publications, 1990).

Bathurst, J. C., "Direct measurements of secondary currents in river bends," Nature **269**, 504–506 (1977).

Blanckaert, K., "Topographic steering, flow recirculation, velocity redistribution, and bed topography in sharp meander bends," Water Resour. Res. **46**(9), W09506, https://doi.org/10.1029/2009WR008303 (2010).

Blanckaert, K., "Flow separation at convex banks in open channels," J. Fluid Mech. **779**, 432–467 (2015).

Blanckaert, K. and de Vriend, H. J., "Secondary flow in sharp open-channel bends," J. Fluid Mech. **498**, 353–380 (2004).

Blanckaert, K. and de Vriend, H. J., "Turbulence characteristics in sharp open-channel bends," Phys. Fluids **17**(5), 055102–055115 (2005a).

Blanckaert, K. and de Vriend, H. J., "Turbulence structure in sharp open-channel bends," J. Fluid Mech. **536**, 27–48 (2005b).

Blanckaert, K. and de Vriend, H. J., "Meander dynamics: A nonlinear model without curvature restrictions for flow in open-channel bends," J. Geophys. Res. **115**, F04011, https://doi.org/10.1029/2009JF001301 (2010).

Blanckaert, K. and Graf, W. H., "Mean flow and turbulence in open channel bend," J. Hydraul. Eng. **127**, 835–847 (2001).

Booij, R., "Measurements and large eddy simulations of the flows in some curved flumes," J. Turbul. **4**(4), 8 (2003).

Bormans, M., Ford, P. W., and Fabbro, L., "Spatial and temporal variability in cyanobacterial populations controlled by physical processes," J. Plankton Res. **27**(1), 61–70 (2004).

Boussinesq, M. J., "Mémoire sur le influence de frottement dans les mouvements réguliers des fluides; XII - Essai sur le mouvement permanent de un liquide dans un canal horizontal a axe circulaire," J. Math. Pure Appl **13**(413), 377–424 (1868).

Chant, R. J. and Wilson, R. E., "Secondary circulation in a highly stratified estuary," J. Geophys. Res. **102**(C10), 23207–23215, https://doi.org/10.1029/97JC00685 (1997).

Cimarelli, A., Leonforte, A., De Angelis, E., Crivellini, A., and Angeli, D., "On negative turbulence production phenomena in the shear layer of separating and reattaching flows," Phys. Lett., Sect. A **383**(10), 1019–1026 (2019).

Constantinescu, G., Koken, M., and Zeng, J., "The structure of turbulent flow in an open channel bend of strong curvature with deformed bed: Insight provided by detached eddy simulation," Water Resour. Res. **47**(5), W05515, https://doi.org/10.1029/2010WR010114 (2011).

Esfahani, F. S. and Keshavarzi, A., "Circulation cells topology and their effect on migration pattern of different multi-bend meandering rivers," Int. J. Sediment Res. **35**(6), 636–650 (2020).

Farhadi, A., Sindelar, C., Tritthart, M., Glas, M., Blanckaert, K., and Habersack, H., "An investigation on the outer bank cell of secondary flow in channel bends," J. Hydro-Environ. Res. **18**, 1–11 (2018).

Ferguson, R. I., "Meander irregularity and wavelength estimation," J. Hydrol. **26**(3–4), 315–333 (1975).

García-Villalba, M. and del Álamo, J. C., "Turbulence modification by stable stratification in channel flow," Phys. Fluids **23**(4), 045104 (2011).

Garg, R. P., Ferziger, J. H., Monismith, S. G., and Koseff, J. R., "Stably stratified turbulent channel flows. I. Stratification regimes and turbulence suppression mechanism," Phys. Fluids **12**(10), 2569–2594 (2000).

Kashyap, S., Rennie, C. D., Townsend, R., Constantinescu, G., and Tokyay, T. E., "Flow around submerged groynes in a sharp bend using a 3D LES model," in *River Flow*, edited by A. Dittrich, Ka. Koll, J. Aberle, and J. Geisenhainer (Bundesanstalt für Wasserbau, 2010), pp. 643–650.

Kim, J. S., Seo, I. W., Baek, D., and Kang, P. K., "Recirculating flow-induced anomalous transport in meandering open-channel flows," Adv. Water Resources **141**, 103603 (2020).

Kirkpatrick, M. P., "A large eddy simulation code for industrial and environmental flows," Ph.D. thesis, The University of Sydney, Sydney, Australia, 2002.

Kirkpatrick, M. P., Williamson, N., Armfield, S. W., and Zecevic, V., "Evolution of thermally stratified turbulent open channel flow after removal of the heat source," J. Fluid Mech. **876**, 356–412 (2019).

Kirkpatrick, M. P., Williamson, N., Armfield, S. W., and Zecevic, V., "Destratification of thermally stratified turbulent open-channel flow by surface cooling," J. Fluid Mech. **899**, A29–A36 (2020).
Komen, E., Camilo, L., Shams, A., Geurts, B., and Koren, B., "A quantification method for numerical dissipation in quasi-dns and under-resolved dns, and effects of numerical dissipation in quasi-dns and under-resolved dns of turbulent channel flows," J. Comput. Phys. **345**(345), 565–595 (2017).
Kranenburg, W. M., Geyer, W. R., Garcia, A. M. P., and Ralston, D. K., "Reversed lateral circulation in a sharp estuarine bend with weak stratification," J. Phys. Oceanogr. **49**(6), 1619–1637 (2019).
Lacy, R. and Monismith, G., "Secondary currents in a curved, stratified, estuarine channel," J. Geophys. Res. **106**, 31283–31302, https://doi.org/10.1029/2000JC000606 (2001).
Leopold, L. B. and Langbein, W. B., "River meander," Sci. Am. **214**(214), 60–73 (1966).
Leopold, L. B. and Langbein, W. B., *Rivers and River Terraces* (Palgrave Macmillan UK, London, 1970).
Moritz, C., Blackall, L., Davis, J., *et al.*, "Investigation of the causes of mass fish kills in the Menindee Region NSW over the summer of 2018–2019," Australian Academy of Science, 2019; available at https://www.science.org.au/supporting-science/science-policy-and-sector-analysis/reports-and-publications/fish-kills-report.
Neary, M. D. and Stephanoff, K. D., "Shear-layer-driven transition in a rectangular cavity," Phys. Fluids **30**(10), 2936 (1987).
Nidzieko, N. J., Hench, J. L., and Monismith, S. G., "Lateral circulation in well-Mixed and stratified estuarine flows with curvature," J. Phys. Oceanogr. **39**(4), 831–851 (2009).
Pein, J., Valle-Levinson, A., and Stanev, E. V., "Secondary circulation asymmetry in a meandering, partially stratified estuary," J. Geophys. Res. Oceans **123**(3), 1670–1683 (2018).
Richmond, M. C., Chen, H. C., and Patel, V. C., "Equations of laminar and turbulent flows in general curvilinear coordinates," Inst. of Hydraulic Research, Iowa Univ., Iowa City, Report No. ADA166837, 1986.
Schwarz, W. R. and Bradshaw, P., "Turbulence structural changes for a three-dimensional turbulent boundary layer in a 30 degrees bend," J. Fluid Mech. **272**, 183–209 (1994).
Segal, G., Vuik, K., and Kassels, K., "On the implementation of symmetric and antisymmetric periodic boundary conditions for incompressible flow," Int. J. Numer. Meth. Fluids **18**(12), 1153–1165 (1994).
Sherman, B. S., Webster, I. T., Jones, G. J., and Oliver, R. L., "Transitions between Aulacoseira and Anabaena dominance in a turbid river weir pool," Limnol. Oceanogr. **43**(8), 1902–1915 (1998).
Thompson, J., "On the origin of windings of rivers in alluvial plains, with remarks on the flow of water round bends in pipes," Proc. R. Soc. London **25**(171–178), 5–8 (1876).
Turner, L. and Erskine, W. D., "Variability in the development, persistence and breakdown of thermal, oxygen and salt stratification on regulated rivers of southeastern Australia," River Res. Appl. **21**(2–3), 151–168 (2005).
van Balen, W., Blanckaert, K., and Uijttewaal, W. S., "Analysis of the role of turbulence in curved open-channel flow at different water depths by means of experiments, LES and RANS," J. Turbul. **11**, N12–N19 (2010).
van Balen, W., Uijttewaal, W. S., and Blanckaert, K., "Large-eddy simulation of a mildly curved open-channel flow," J. Fluid Mech. **630**, 413–442 (2009).
Vant, W. N., *Lake Managers Handbook: A Guide to Undertaking and Understanding Investigations into Lake Ecosystems, so as to Assess Management Options for Lakes* (Published for the National Water and Soil Conservation Authority by the Water and Soil Directorate, Ministry of Works and Development, Wellington, NZ, 1987).
Williamson, N., Armfield, S. W., Kirkpatrick, M. P., and Norris, S. E., "Transition to stably stratified states in open channel flow with radiative surface heating," J. Fluid Mech. **766**, 528–555 (2015).
Williamson, N., Norris, S. E., Armfield, S. W., and Kirkpatrick, M. P., "Lateral circulation in a stratified open channel on a 120 degree bend," Water Resour. Res. **48**(12), W12512, https://doi.org/10.1029/2012WR012218 (2012).